Dalton Transactions

ROYAL SOCIETY OF CHEMISTRY

PAPER

View Article Online
View Journal | View Issue

Cite this: *Dalton Trans.*, 2025, **54**, 1850

Terpyridine-based ruthenium complexes containing a 4,5-diazafluoren-9-one ligand with light-driven enhancement of biological activity†

Francisca Mayara Santos de Alencar,[a] Florencio Sousa Gouveia, Jr.,[a] Geângela de Fátima Sousa de Oliveira,[a] Alexandre Lopes Andrade,[b] Mayron Alves de Vasconcelos,[c] Alejandro Pedro Ayala,[d] Ana Claudia Silva Gondim,[a] Idalina Maria Moreira de Carvalho,[a] Carlos André Ferreira Moraes,[e] Marcos V. Palmeira-Mello,[e] Alzir Azevedo Batista,[e] Luiz Gonzaga de França Lopes *[a] and Eduardo Henrique Silva Sousa *[a]

There has been growing effort in the scientific community to develop new antibiotics to address the major threat of bacterial resistance. One promising approach is the use of metal complexes that provide broader opportunities. Among these systems, polypyridine-ruthenium(II) complexes have received particular attention as drug candidates. Here, we prepared two new ruthenium(II) complexes with the formulation [Ru(DFO)(phtpy-R)Cl](PF$_6$), where phtpy = 4′-phenyl-2,2′:6′,2″-terpyridine; R = −H(**MPD1**), −CH$_3$(**MPD2**); and DFO = 4,5-diazafluoren-9-one, and investigated their chemical, biochemical and antibacterial activities. These compounds exhibit photoreactivity and produce reactive oxygen species (ROSs). Photogeneration of singlet oxygen ($^1O_2$) was measured in acetonitrile with significant quantum yields using blue light, Φ = 0.40 and 0.39 for **MDP1** and **MPD2**, respectively. Further studies have shown that **MPD1** and **MPD2** can generate superoxide radicals. Antibacterial assays demonstrated a significant enhancement in MIC (minimum inhibitory concentration) upon blue light irradiation (>32-fold), with MICs of 15.6 μg mL^{-1} (*S. aureus*, ATCC 700698) and 3.9 μg mL^{-1} (*S. epidermidis*, ATCC 35984) for both metal complexes. Interestingly, an MIC of 15.6 μg mL^{-1} for **MPD1** and **MPD2** was observed against *S. epidermidis* ATCC 12228 under red light irradiation. The latter results are encouraging, considering that red light penetrates deeper into the skin. In addition, no significant cytotoxicity was observed in some mammalian cells, even upon light irradiation, supporting their potential safety. Altogether, these data show evidence of the potential use of these compounds as antimicrobial photodynamic therapeutic agents, enriching our arsenal to combat this worldwide bacterial threat.

Received 9th September 2024,
Accepted 4th December 2024

DOI: 10.1039/d4dt02562h

rsc.li/dalton

Introduction

Antimicrobial agents are drugs used to prevent and treat infections in humans, animals, and even plants.[1] There is, currently, significant concern about the growing number of resistant bacteria that annually cause *ca.* 700 000 deaths worldwide, whose situation may worsen after the indiscriminate use of antibiotics in the pandemic period of COVID-19.[2–4] The continuous excessive and undue use of antibiotics is expected to lead to 10 million people deaths annually from drug-resistant bacterial infections over the next 35 years.[5] Evidently, this is going to make treatment of these infections even more difficult to be carried out, increasing the risk of infections, dissemination of diseases, occurrence of severe forms of diseases, and even more deaths.[6]

There is already a major concern for the rapid global spread of multidrug-resistant (MDR) and pan-drug resistant (PDR)

[a]*Group of Bioinorganic, Department of Organic and Inorganic Chemistry, Federal University of Ceara, Fortaleza, Brazil. E-mail: eduardohss@dqoi.ufc.br, lopeslu@dqoi.ufc.br*
[b]*Integrated Biomolecular Laboratory, Department of Pathology and Legal Medicine, Federal University of Ceara, Fortaleza, Brazil*
[c]*Faculdade de Educação de Itapipoca, Universidade Estadual do Ceará, Itapipoca, CE, Brazil*
[d]*Department of Physics, Federal University of Ceara, Fortaleza, Brazil*
[e]*Department of Chemistry, Federal University of São Carlos, 13565-905 São Carlos, SP, Brazil*

†Electronic supplementary information (ESI) available. CCDC 2375482 and 2375481. For ESI and crystallographic data in CIF or other electronic format see DOI: https://doi.org/10.1039/d4dt02562h

bacteria, as reported by the World Health Organization (WHO).[1] The latter strain does not respond to any class of antibiotics available, representing an immediate threat. For example, glycopeptide-resistant Gram-negative bacteria are resistant to all available antimicrobials, including tigecycline and colistin drugs.[7] It is essential to develop new antibacterial compounds that can circumvent these mechanisms of resistance. At the end of 2023, new antibiotic candidates with novel mechanisms of action caught the attention of the scientific community because of their efficacy against carbapenem-resistant *Acinetobacter baumannii*, a highly resilient opportunistic bacterium found in hospital settings, where some had just entered clinical trials.[8,9] This case reminds us of the urgent need for antibiotic compounds, particularly with novel mechanisms of action. Inorganic-based compounds, or even nanomaterials, have shown promising activity against bacteria, including antibiotic-resistant bacterial strains, which may help in dealing with this issue and also delay the emergence of further resistance.[10] These types of compounds can also offer new mechanisms of action targeting many distinct biological targets opening great opportunities.[11,12]

There is a need to develop new non-toxic antimicrobial technologies that can act more effectively and quickly than the current antibiotics. Such innovations include the use of inorganic compounds in antiproliferative materials such as clusters,[13] photocatalytic metal–organic frameworks (MOFs),[14–16] conjugated polymers,[17] and microphysiological systems (MPSs),[18] among others. In these examples, they show a remarkable sterilization effect under conditions of ROS generation upon light irradiation. In addition to the aforementioned materials, an effective technology is antimicrobial photodynamic therapy (aPDT).[19] This relies on causing bacterial cell death in the presence of a photosensitive compound (PS) that promotes local and temporal generation of reactive oxygen species through light excitation.[20–22] Several studies have shown the application of aPDT in clinical treatments, such as in the repair of diabetic wounds,[23,24] dermatological treatments,[25] bacterial biofilm control, and[26] pre-treatment of catheters in hospital settings,[27,28] among others.

The effectiveness of aPDT depends mainly on some factors, including the use of adequate PS compounds, which must present high phototoxicity, low toxicity in the dark, a high quantum yield of $^1O_2$ (and/or other deleterious free radicals), adequate pharmacokinetics, uptake by bacteria, or interaction with the bacterial cell membrane/wall.[29] There is availability of light probe devices for virtually any part of the body, which has broadened the opportunities for phototherapy. The use of metal complexes as potential PS drugs has been widely studied owing to their promising photochemical and photophysical processes. One of the oldest compounds exhibiting promising photogeneration of ROSs was the tris(2,2′-bipyridine)ruthenium(II) ion, and a series of other polypyridine complexes have been investigated since then. The polypyridine ruthenium compound TLD1443 has been investigated as a PDT agent, which is in phase 2 clinical trials against non-muscle-invasive bladder cancer.[30,31]

In the development of novel metal compounds, a metal center can be combined with distinct ligands to achieve the desired properties for use as a therapeutic agent. Metal complexes containing substituted phenyl-terpyridine polypyridine derivatives or 4,5-diazafluoren-9-one (DFO) ligands exhibit interesting physicochemical and biological properties, making these types of ligands relevant in this design. Among the properties described for some of these compounds, one can mention a few that stand out, such as antibacterial action,[32,33] antiproliferative cell activity,[34–38] and DNA interaction and photocleavage,[39,40] among others.

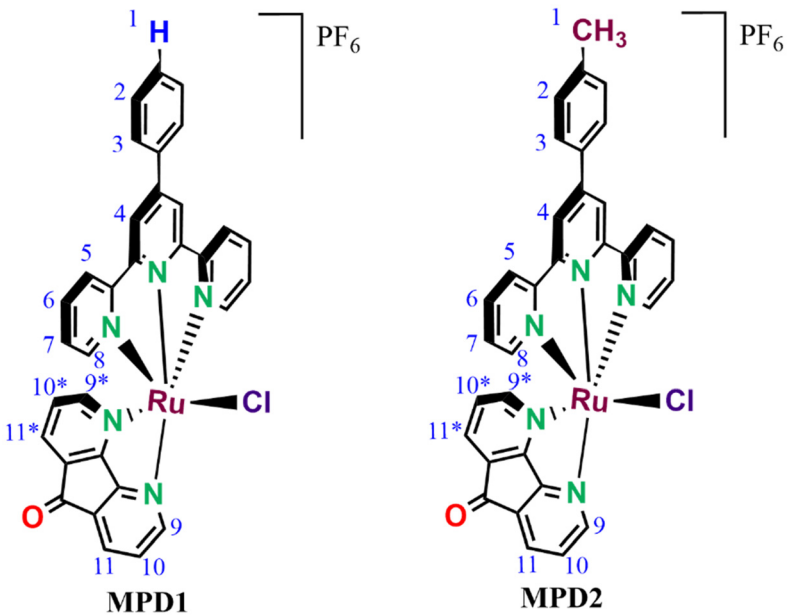

Fig. 1 Structures of **MPD1** and **MPD2**.

Having this in mind, we combined these ligands and prepared two new polypyridine ruthenium complexes, aiming to achieve ROS ($^1O_2$) photoproduction along with the capacity to eliminate bacteria (Fig. 1). The organic ligands employed may assist in the generation of ROSs, while terpyridine-derived ligands could particularly promote an absorption red-shift due to their increased π conjugation, thus, possibly achieving close to the phototherapeutic window (600–850 nm).[41] Interestingly, these compounds exhibited promising biological activities against Gram-positive bacteria with enhanced action upon light irradiation, even upon irradiation with red light, as further described.

Results and discussion

Syntheses of the metal complexes

The metal complexes [Ru(DFO)(phtpy)Cl](PF$_6$) (**MPD1**, where phtpy = 4′-phenyl-2,2′:6′,2″-terpyridine and DFO = 4,5-diazafluoren-9-one) and [Ru(DFO)(phtpyMe)Cl](PF$_6$) (**MPD2**, where phtpyMe = 4′-(*p*-tolyl)-2,2′:6′,2″-terpyridine and DFO = 4,5-diazafluoren-9-one) were obtained through procedures described in the Experimental section. In summary, they were synthesized in three steps, starting from the precursor *cis*-[Ru(DMSO)$_4$Cl$_2$], in which three DMSO ligands were replaced by one terpyridine derivative ligand. This new precursor, *cis*-[Ru(phtpy-R)(DMSO)Cl$_2$], had one chlorido ligand and one DMSO ligand replaced by a 4,5-diazafluoren-9-one (DFO) ligand, which was further isolated as a PF_6^- salt. These metal complexes were fully characterized using spectroscopic and electrochemical techniques, and supported by computational calculations as shown further.

Characterization

Red crystals of the metal complexes **MPD1** and **MPD2** were obtained by slow evaporation of an acetone/ethyl ether solution at 28 °C and protected from light. These crystals were suitable for single-crystal X-ray diffraction analyses. All crystallographic data and structure refinement parameters are summarized in Table 1.

The **MPD1** and **MPD2** compounds crystallized into two distinct crystalline systems, monoclinic ($P2_1/c$) and triclinic ($P\bar{1}$), respectively. The asymmetric unit cell is shown in Fig. 2 with the atom-labeling scheme employed. These structures are consistent with the formulation of the metal complexes as a monomeric six-coordinated molecular species, where the ligands show *trans* geometry for the Cl^- ligand in relation to the DFO ligand. Table 2 summarizes all relevant interatomic bond lengths and bond angles for **MPD1** and **MPD2**, respectively. The presence of one PF_6^- counterion supports a Ru(II) charge in both structures in agreement with NMR and elemental analyses. In the case of **MPD1**, acetone, as a crystallization solvent, was incorporated into the crystalline structure.

^{1}H NMR spectra showed signal patterns consistent with the coordination of all chelating ligands (Fig. 3A and Fig. S1, ESI†), while bidimensional NMR techniques (COSY and HSQC) (Fig. 3B and Fig. S2–S3, ESI†) were suitable for assisting on the full assignment of the hydrogen signals. **MPD1** showed integration signals for 21 hydrogens as expected when a triplet signal at 7.61 ppm was integrated for 1 hydrogen. This signal was assigned to H-1 as depicted in Fig. 1, while another signal at 9.18 ppm was attributed to H-4 of that metal complex.[42]

Further characterization employing ^{13}C NMR showed signals of the aromatic ligands from 120 to 150 ppm as expected for the sp^2 carbons of the DFO and terpyridine-based ligands. We observed 22 and 23 signals of carbons for the **MPD1** and **MPD2** complexes, respectively. These hydrogen integrations and carbon signals were consistent with the formulation proposed and the symmetry present in the phtpy-R ligand. One typical signal of the carbonyl group of DFO was observed at 187 ppm, which is noticed for the **MPD1** and **MPD2** complexes.[43,44] The carbon signals for the phtpy ligand were found in a similar region to what was reported in the literature for analogous metal compounds with small changes in the chemical shift (δ).[45] Table S1, ESI† resumes all attributions

Table 1 Crystallographic data refinement for **MPD1** and **MPD2**

	MDP1	**MDP2**
CCDC number	2375482	2375481
Empirical formula	$C_{32}H_{21}ClN_5ORu$, PF_6, $1.5(C_3H_6O)$	$C_{33}H_{23}ClN_5ORu$, PF_6, $0.5[H_2O]$
Formula weight	860.14	796.06
Temperature [K]	300.00	150.00
Crystal system	Monoclinic	Triclinic
Space group	$P2_1/c$(14)	$P\bar{1}$(2)
a [Å]	8.7628(7)	8.746(2)
b [Å]	27.6833(18)	13.317(3)
c [Å]	14.6097(12)	13.892(4)
α [°]	90	96.811(9)
β [°]	95.034(3)	98.431(8)
γ [°]	90	99.510(8)
Volume [Å^3]	3530.4(5)	1561.5(7)
Z	4	2
ρ_{calc} [g cm^{-3}]	1.618	1.693
μ [mm^{-1}]	0.641	0.714
F(000)	1736	798
Crystal size [mm^3]	0.15 × 0.136 × 0.066	0.294 × 0.171 × 0.12
Crystal colour	Dull reddish red	Dull reddish red
Crystal shape	Block	Block
Radiation	MoK$_\alpha$ (λ = 0.71073 Å)	MoK$_\alpha$ (λ = 0.71073 Å)
2θ range [°]	4.06 to 50.70 (0.83 Å)	4.64 to 50.70 (0.83 Å)
Index ranges	$-10 \le h \le 10$ $-33 \le k \le 33$ $-17 \le l \le 17$	$-10 \le h \le 10$ $-16 \le k \le 16$ $-16 \le l \le 16$
Reflections collected	85 572	42 556
Independent reflections	6474 R_{int} = 0.1322 R_{sigma} = 0.0510	5720 R_{int} = 0.1293 R_{sigma} = 0.0844
Completeness	99.9%	99.8%
Data/restraints/parameters	6474/27/497	5720/519/498
Goodness-of-fit on F^2	1.095	1.074
Final R indexes [$I \ge 2\sigma(I)$]	R_1 = 0.0482 wR_2 = 0.0979	R_1 = 0.1165 wR_2 = 0.2466
Final R indexes [all data]	R_1 = 0.0785 wR_2 = 0.1158	R_1 = 0.1820 wR_2 = 0.2959
Largest peak/hole [e Å^{-3}]	0.54/−0.49	1.98/−1.35

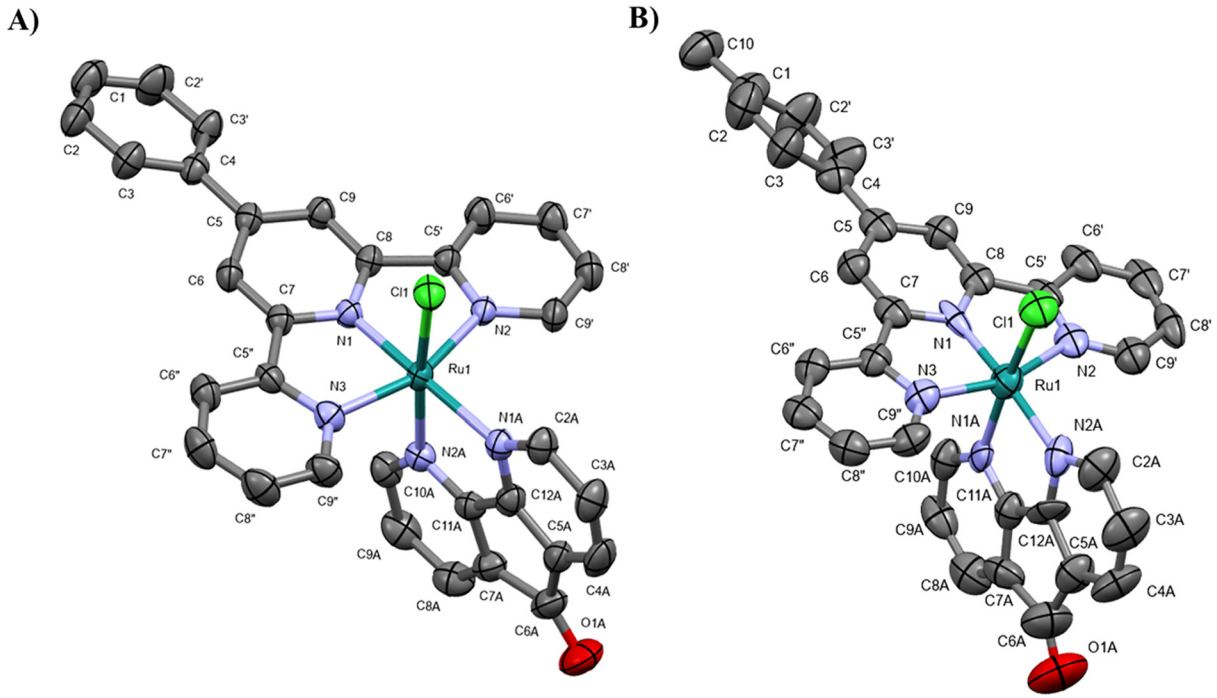

Fig. 2 ORTEP plots of the asymmetric units of **MPD1** (A) and **MPD2** (B) complexes; all computed H atoms, acetone and PF_6^- ions are omitted for clarity.

Table 2 Selected bond lengths (Å) and bond angles (°) of **MPD1** and **MPD2** complexes

MPD1				MPD2			
Bond lengths		Bond angles		Bond angles		Bond angles	
Ru1–Cl1	2.3852(13)	N1–Ru1–N1A	177.81(15)	Ru1–Cl1	2.382(4)	N1–Ru1–N2A	174.1(4)
Ru1–N1	1.934(4)	N2–Ru1–N3	159.67(15)	Ru1–N1	1.887(12)	N2–Ru1–N3	159.7(5)
Ru1–N2	2.064(4)	N2A–Ru1–Cl1	173.38(11)	Ru1–N2	2.063(11)	N1A–Ru1–Cl1	172.4(3)
Ru1–N3	2.067(4)	N1–Ru1–N2	79.84(15)	Ru1–N3	2.063(11)	N1–Ru1–N2	79.0(4)
Ru1–N1A	2.128(4)	N1–Ru1–N3	79.84(15)	Ru1–N1A	2.130(11)	N1–Ru1–N3	80.7(4)
Ru1–N2A	2.102(4)	N1A–Ru1–N2A	82.12(15)	Ru1–N2A	2.070(11)	N1A–Ru1–N2A	83.0(4)
N2–C5′	1.373(6)	C3′–C4–C5	121.7(4)	N2–C5′	1.382(17)	C3′–C4–C5	121.7(14)
N3–C5″	1.367(6)	Ru1–N3–C5″	113.2(3)	N3–C5″	1.345(16)	Ru1–N3–C5″	112.7(9)
N1A–C2A	1.359(6)	Ru1–N1–C8	119.5(3)	N1A–C10A	1.333(16)	Ru1–N1–C8	124.2(9)
N2A–C10A	1.343(6)	Ru1–N1A–C12A	108.8(3)	N2A–C2A	1.343(17)	Ru1–N2A–C12A	107.6(8)
C6A–O1A	1.191(6)	N1–Ru1–Cl1	90.43(12)	C6A–O1A	1.12(2)	N1–Ru1–Cl1	95.8(3)

of ^{13}C NMR for this compound. Fig. S2 and S3 ESI† illustrate the ^{13}C NMR spectrum for **MPD1**, and Table S2, ESI† summarizes all assignments of the signals observed. Once these two metal compounds are very similar, but for a methyl residue, the similarity in all assignments is not surprising, while **MPD2** showed an extra carbon signal at 21.5 ppm, characteristic of an sp^3 carbon. In addition, a signal of C-1 of the ring D (Fig. S2 and S3, ESI†) was seen with the signal at 140.38 ppm, characteristic of *ortho–para* substituted benzenic rings.

High-resolution mass spectrometry (ESI-MS) was performed by direct infusion, in a mobile phase containing 5% H_2O (solvent A, 0.1% formic acid) and 95% acetonitrile (solvent B with 0.1% formic acid). These measurements showed an interesting profile (Fig. S4, ESI†) in which the intact molecular ion was found with an m/z value of 628.0497 u (theoretical 628.0473 u, $[M + H - PF_6]^+$) for **MPD1** and an m/z value of 642.0628 u (theoretical 642.0629 u, $[M + H - PF_6]^+$) for **MPD2** (Fig. S4, ESI†), which were fully consistent with the proposed structures.

Density functional theory (DFT) was used to optimize the geometry of **MPD1** and **MPD2** and also calculate their vibrational and electronic spectra. This theoretical FTIR spectrum agreed with the experimental data, thus supporting our vibrational mode assignments. Fig. S5, ESI† shows these data and illustrates their satisfactory agreement. The experimental FTIR spectra of the **MPD1** and **MPD2** complexes showed characteristic bands of ruthenium complexes supporting the presence of DFO (*e.g.*, ν(C═O) at 1735 and 1737 cm^{-1}, for

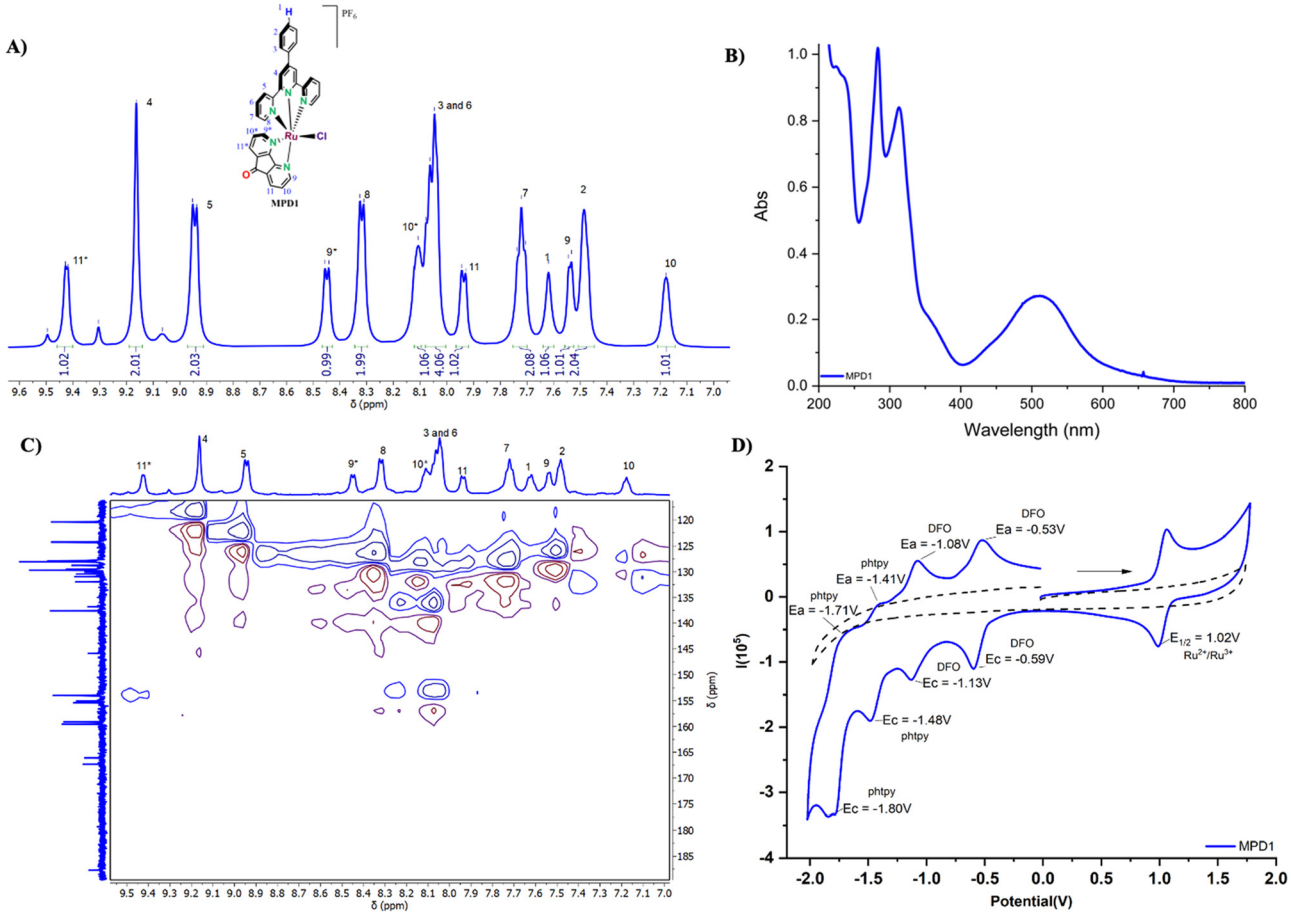

Fig. 3 **MPD1** characterization: (A) ^{1}H NMR in $(CD_3)_2SO$; (B) electronic absorption spectra in acetonitrile (3×10^{-5} mol L^{-1}) at 25 °C; (C) HSQC NMR in $(CD_3)_2SO$; (D) cyclic voltammogram in 0.1 mol L^{-1} $TBAPF_6$/acetonitrile at 25 °C, at a scan rate of 0.100 V s^{-1}, using glassy carbon, platinum wire and Ag|AgCl as working, auxiliary and reference electrodes, respectively (a ferrocene redox pair used as a reference). The black dashed line represents a sweep potential for the electrolyte solution only.

MPD1 and **MPD2**, respectively) and phtpy and derivative ligands, indicating their coordination to the metal center (Table S3, ESI†). Additionally, two strong bands at *ca*. 850 and *ca*. 557 cm^{-1} were seen in both metal complexes, which were assigned to axial and angular deformation modes for hexafluorophosphate found as a counterion.

We investigated the redox processes of these metal complexes by cyclic voltammetry using a glassy carbon working electrode in a 0.1 mol L^{-1} solution of tetrabutylammonium hexafluorophosphate in acetonitrile at 25 °C. These metal complexes showed a series of redox processes in a wide range of potentials from −2.3 V up to +1.8 V. **MPD1** and **MPD2** showed *quasi*-reversible redox processes at +1.02 V and +0.94 V *vs.* Ag|AgCl (Fig. 3D and Fig. S1, ESI†), respectively, which corresponded to the $Ru^{III/II}$ redox process.

In addition, four redox waves were observed at negative potentials, which are associated with the aromatic ligands (Fig. S6, ESI†). The first two redox pairs with E_c values of −0.59 V and −1.13 V for **MPD1**, as well as −0.66 V and −1.22 V for **MPD2**, were attributed to the DFO ligand (Fig. S6, ESI†). The third and fourth irreversible cathode waves were associated with processes characteristic of phenyl-terpyridine ligands as summarized at −1.48 V and −1.80 V for **MPD1** and also at −1.56 V and −1.87 V for **MPD2** depicted in Table 4. These ligand-based processes have been previously reported in the literature, both for phenyl-terpyridine derivatives[46–50] and the DFO ligand,[47,51] but never combined in the same ruthenium (II) complex. The redox potentials for **MPD2** shifted by 80 mV is likely due to the inductive effect of the methyl moiety allowing better stabilization of the Ru(III) state.

An examination of the frontier molecular orbital composition using DFT data for the **MPD1** and **MPD2** complexes (Fig. 4) indicated a significant contribution of the DFO ligand. This was experimentally supported by the fact that the first redox process in the negative region of the voltammogram is indeed characteristic of this ligand in both metal complexes.

Electronic spectra of both metal complexes were recorded in acetonitrile (Fig. 3B and Fig. S1, ESI†) (Table 4). There are four high-energy electronic transition bands with maxima at 231, 283, 314, and 364 nm for **MPD1**, while for **MPD2** there were minor changes in these bands with maxima at 257, 276, 310, and 364 nm. It is important to remark that the energies

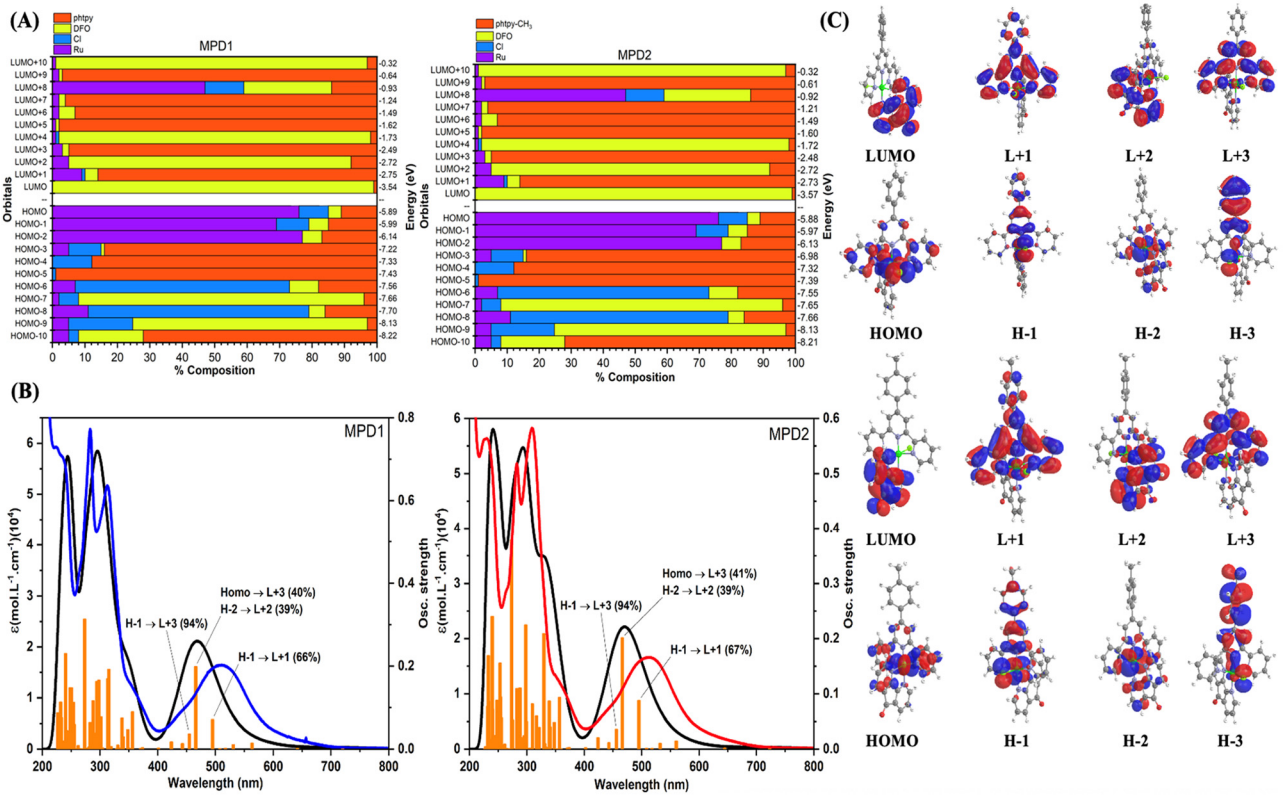

Fig. 4 DFT and TD-DFT calculations of the percentage contribution of the Cl^{-}, DFO, phtpy, phtpy-CH_3, and Ru fragments of selected molecular orbitals of **MPD1** and **MPD2** (A). Experimental and simulated and absorption spectra of **MPD1** and **MPD2** (B). Selected molecular orbitals for the ion complex **MPD1** consistent with their major UV–Vis electronic transitions using TD-DFT (C).

and intensities of these bands resemble those of the free ligands (Fig. S7, ESI†). This result suggests that these electronic transitions are still primarily localized within the aromatic ligands and may be analogous to the type of transition reported for the free ligands. Besides these bands, **MPD1** and **MPD2** also displayed broad bands in the visible range exhibiting peaks at 510 nm and 513 nm, respectively. These bands are attributed to metal-to-ligand charge transfer (MLCT) transitions as supported by TD-DFT calculations. Indeed, these bands are commonly reported in polypyridine-derived metal complexes[48] and ruthenium(II) complexes with aromatic N-heterocyclic ligands, displaying a strong absorption band in the visible range with a molar extinction coefficient (ε) of approximately 10^4 mol^{-1} L cm^{-1}.[52] Molecular orbital (MO) contribution analysis was used primarily to support interpretation of the spectroscopic behavior of the metal complexes. An attempt to assign these transition bands was also made and all assignments are presented in Tables S4 and S5, ESI.†

Calculations were performed to gain insights into the electronic structures of **MPD1** and **MPD2**. The geometry of these compounds was fully optimized at the B3LYP/6-31G level. DFT calculations revealed that the ground state HOMO of **MPD1** is mainly formed by the dπ-bonding orbital of the ruthenium moiety (76%), while the LUMO is mainly located on the π-antibonding orbital of the DFO ligand (99%), whereas **MPD2** showed a similar profile (Fig. 4A–C). This profile is consistent with our assignment for the first two reduction processes being centered on the DFO ligand. In addition, the process in the positive range associated with the ruthenium moiety is also consistent with the distribution of the HOMO on the ruthenium. Interestingly, the LUMO+1 and LUMO+2 of **MPD1** are distributed mainly over phtpy (87%) and DFO (88%), respectively. This profile was very similar for **MPD2**, where the LUMO+1 and LUMO+2 are also distributed mainly over phtpy (86%) and DFO (87%), respectively (Fig. 4C). Although the calculated HOMO energies for **MPD1** and **MPD2** are very close, their electrochemical potentials were reasonably distinct indicating that even a moderate change in phtpy can still cause expressive electronic disturbances.

Partition coefficient

The size, spatial orientation, charge and lipophilicity of a molecule are key factors involved in the uptake and cellular distribution, which becomes important during drug development.[53] The partition coefficient ($\log P$) and the distribution coefficient ($\log D$) measure the distribution of a compound in water and buffered media compared to an organic solvent (octanol). This parameter plays an important role in indicating its potential passive absorption by cells. Based on this, we measured the lipophilicity of our metal complexes in which **MPD1** and **MPD2** exhibited $\log P$ values of −0.11(±0.03) and −0.23(±0.08), respectively, while they exhibited $\log D_{7.4}$ values

Table 3 Experimental data for metal complexes **MPD1** and **MPD2**

Metal complex	λ_{max} [a]/nm ($\varepsilon \times 10^4$/mol L^{-1} cm^{-1})	E [b] (V *vs.* Ag|AgCl) $Ru^{III/II}$ $E_{1/2}$	R-phtpy/DFO ligands	Singlet oxygen quantum yield (Φ_Δ)[c] SOSG H_2O	SOSG MeOH	DPBF ACN	DPBF MeOH	Log P[d]	Log D pH 7.43 [a]
MPD1	283 (2.01), 313 (1.63), 365 (0.19), and 491 (0.49)	+1.02	E_c: −0.59, −1.13, −1.48, and −1.80 E_a: −0.53, −1.08, −1.41, and −1.71	0.04	0.13	0.40	0.17	−0.11 (±0.03)	−0.41 (±0.03)
MPD2	284 (1.92), 311 (2.31), 365 (0.26), and 493 (0.67)	+0.94	E_c: −0.66, −1.22, −1.56, and −1.87 E_a: −0.58, −1.15, −1.50, and −1.77	0.06	0.17	0.39	0.12	−0.23 (±0.08)	−0.17 (±0.04)

[a] Solvent: PBS buffer 0.1 mol L^{-1} pH 7.4 at 25 °C. [b] Solvent: acetonitrile. [c] Upon blue light irradiation, λ_{exc} = 410 nm and Φ_Δ = 0.84 for $[Ru(bpy)_3]^{2+}$ in methanol. MeOH = methanol; ACN = acetonitrile. [d] Solvent: H_2O.

of −0.41(±0.03) and −0.17 (±0.04), for **MPD1** and **MPD2**, respectively (Table 3). These compounds are considered slightly hydrophilic (−0.3 < log P < 0). Lipophilicity is crucial when studying the interactions of Ru(II) complexes with biological systems, with ideal values of log P ranging from 2 to 5, since high lipophilicity improves cellular uptake by increasing interactions with intracellular biomolecules as well.[54] However, water solubility is also important for effective pharmacokinetic processes. Hydrophilic drugs can also take advantage of facilitated transport across cell membranes using specific transporters.[55] Furthermore, there are many hydrophilic approved drugs outside the ideal range of log P and log D values, which does not limit this study.

Thermal and photochemical stability measurements

The thermal and photochemical stability of the metal complexes was studied in different solvents (Tris-HCl buffer, DMSO, acetonitrile, and ethanol) in the absence of or upon irradiation with blue light (Fig. S8 and S9, ESI†). At the end of the monitoring period of up to 24 h, it was not possible to observe any significant changes in the electronic spectra of the metal complexes. These results would indicate a lack of reactions or exchange of the ligands supporting their stability under those conditions. Interestingly, similar behavior was also observed upon light irradiation, demonstrating significant photochemical stability for these metal complexes as well.

Photogeneration of reactive oxygen species (ROSs)

Singlet oxygen production ($^1O_2$). Considering that $^1O_2$ is an important biocidal species, any attempt to develop phototherapeutic agents commonly evaluates its production. For the metal complexes **MPD1** and **MPD2**, blue light irradiation measurements were performed to investigate whether or not singlet oxygen generation was achieved and calculate the quantum yield (Φ_Δ), which was also explored using red light irradiation. We should mention that topical treatment or even internal use of light probes can still allow the efficient use of phototherapy even outside the desirable phototherapeutic window (600–900 nm).[56]

Initially, a DPBF probe was used to detect singlet oxygen species, and even though it is less selective, we can use it with many types of solvents including less suppressive ones to the generation of $^1O_2$ species.[57] In addition to that, Singlet Oxygen Sensor Green (SOSG), a highly selective probe for $^1O_2$ species, was also employed as a fluorometric probe, and it could be used in aqueous media and some organic solvents as well (*e.g.*, methanol). The latter probe works through an intramolecular photoinduced electron transfer (PET) process to detect $^1O_2$, where one moiety consists of an electron donor portion (derived from anthracene) and another consists of a covalently linked acceptor. In the presence of $^1O_2$, a reaction occurs with the anthracene ring forming endoperoxide-anthracene that quenches intramolecular PET allowing the emission of light.[58] On the other hand, the fluorescent DPBF probe upon reaction with $^1O_2$ species is converted into a non-fluorescent product. In both assays, standard singlet oxygen generators were used as reference compounds to measure the relative quantum yield (Φ_Δ) (Table 3).

Using DPBF, **MPD1** and **MPD2** in methanol, with blue LED irradiation, promoted low singlet oxygen production with Φ_Δ values of 0.17 and 0.12, respectively (Fig. S10, ESI†). Similar studies with SOSG showed close values of Φ_Δ at 0.13 and 0.17 for **MPD1** and **MPD2**, respectively. These results showed a consistent production of highly reactive species in methanol (Table 3 and Fig. 5) with modest differences between these probes.[57,59] Unfortunately, both metal compounds showed negligible singlet oxygen production in water (Φ_Δ values of 0.04 and 0.06 for **MPD1** and **MPD2**, respectively), which is commonly seen due to the suppressive behavior of water. Nonetheless, we might expect that these compounds are able to produce this type of ROS in other physiological microenvironments. This remark can be supported by measurements carried out in a non-protic solvent (acetonitrile), where the DPBF probe showed an expressive enhancement in the photogeneration of singlet oxygen upon blue light irradiation with

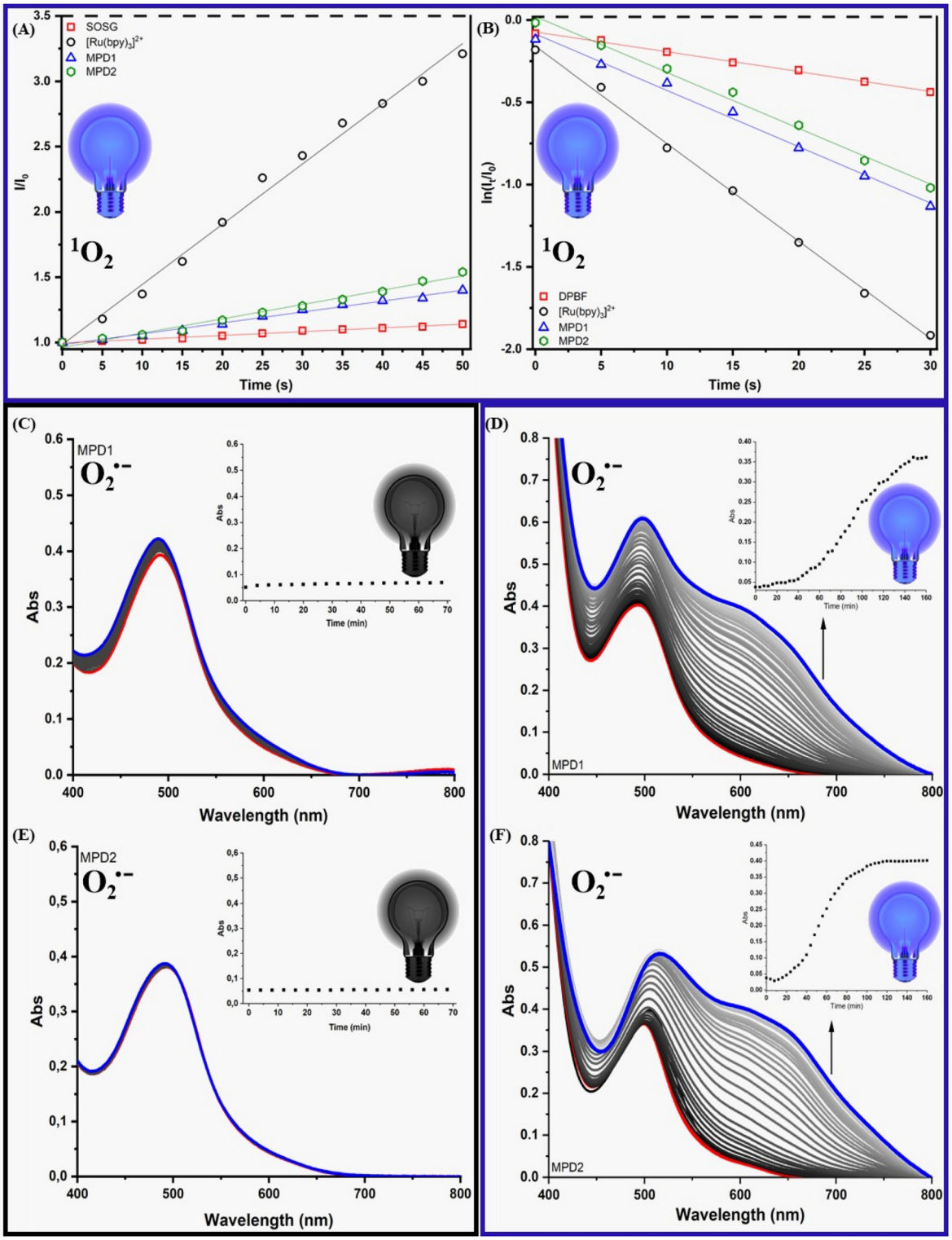

Fig. 5 Investigation of the production of reactive oxygen species as singlet oxygen and superoxide. Singlet oxygen measurements are shown in panels (A) and (B) with time-dependent curves for quantum yield measurements of **MPD1** and **MPD2** samples irradiated with blue light. Panel (A) shows the study using the SOSG probe in methanol, while panel (B) shows an analogous study using the DPBF probe in acetonitrile. Both assays used $[Ru(bpy)_3]^{2+}$ as a standard singlet oxygen photoproducer with blue light. The red squares are SOSG or DPBF only, blue triangles are **MPD1**, green diamonds are **MPD2**, and black circles are $[Ru(bpy)_3]^{2+}$ (Φ_Δ = 0.84, in acetonitrile and Φ_Δ = 0.87, in methanol) all under blue light irradiation at 25 °C. Measurement of superoxide radical production using a reaction mixture of **MPD1** or **MPD2** (at 35 μmol L^{-1}), in PBS 0.1 mol L^{-1}, pH 7.4, reduced glutathione (GSH at 1.5 mmol L^{-1}), NBT (50 μmol L^{-1}) at 25 °C, was investigated under the following conditions: (C) **MPD1** mixed with GSH and NBT and kept in the dark; (D) **MPD1** mixed with GSH and NBT and then irradiated with blue light; (E) **MPD2** mixed with GSH and NBT and then kept in the dark; and (F) **MPD2** mixed with GSH and NBT and then irradiated with blue light.

Φ_Δ values of 0.40 and 0.39 for **MPD1** and **MPD2**, respectively, (Table 3 and Fig. S10, ESI†). In case these compounds are irradiated with red light, in acetonitrile, the Φ_Δ values of 0.10 and 0.05 were still measurable for **MPD1** and **MPD2**, respectively. The latter result is quite encouraging despite the lower production of $^1O_2$.

Hydroxyl radical production (HO$^\bullet$). Another important ROS is the hydroxyl radical, which can be produced through a photochemical type I mechanism involving photoinduced electron transfer processes. The measurement of this radical can be done using aminophenyl fluorescein (APF), a selective fluorescent probe for this radical. However, we and others noticed that this probe can still be sensitive to singlet oxygen radicals making us explore the use of a hydroxyl radical suppressor during these assays as well. Thus, D-mannitol was employed as such a suppressor, enabling us to better identify the contribution of this radical, if any. Our results showed that **MPD1** did not produce any significant hydroxyl radical, while **MPD2** showed only very modest photogeneration of this species. These results supported that singlet oxygen is still the likely major photogenerated product (Fig. S11, ESI†).

Superoxide generation assay. Although being a weaker oxidant species, the $O_2^{\bullet-}$ superoxide radical can still cause serious damage to many biomolecules, particularly by reducing free metals and assisting in the production of other deleterious radical species.[60] Actually, there are many metal complexes capable of producing this radical chemically or photochemically as a biocidal agent. Here, we used nitrotetrazolium blue (NBT) as a colorimetric probe to detect superoxide ions. This yellow probe, NBT, is converted into a blue formazan product upon reaction with superoxide, and this final product can be measured using its light absorption at *ca.* 560–590 nm.[61] Here, we carried out these measurements using 50 μmol L^{-1} NBT and 35 μmol L^{-1} metal complexes. Aiming to evaluate the role of reducing agents during the production of superoxide, we carried out these experiments with and without reduced glutathione (GSH, at 1.5 mmol L^{-1}) (Fig. 5). Once this reducing agent is found at millimolar concentrations within cells, it is a suitable reagent to be employed and commonly explored in this process. Additionally, these metal complexes were also irradiated with blue light or kept in the dark during these experiments. All of these measurements were done in buffered solution at 25 °C.

Although the metal complexes exhibited absorption close to the formazan absorption band, there is clear evidence of the formation of this radical. However, it was only produced if the metal complex was mixed with reduced glutathione (GSH) and also irradiated with blue light (Fig. 5C–F). There is no measurable superoxide production or direct reaction involving the metal compounds and reduced glutathione, in spite of the latter being a common stimulus for the catalytic production of superoxide mediated by many metal complexes even in the dark.[62] Thus, the use of blue light was also a strict requirement for superoxide production along with reduced glutathione, suggesting that a type I mechanism of photoproduction of ROSs takes place.

In particular, **MPD1** and **MPD2** showed a significant capacity to photogenerate superoxide ions, where a typical visual color change was noticed with an eventual purple precipitate in the cuvette at the end of the experiment. **MPD2** showed better photogeneration of this radical, which can be noticed by its faster photogeneration (*ca.* half the time) in comparison with **MPD1** (Fig. 5). A series of controls were done to further support this process (*e.g.*, MPD1/MPD2 + NBT + light; MPD1/MPD2 + GSH; NBT + GSH + light), where we discarded any direct reaction of NBT with glutathione or light or even the metal complex in the absence of NBT as well (Fig. S12, ESI†).[63] Fig. S13, ESI† shows the profile of the initial rate of NBT reduction in the presence of NBT and GSH at increasing concentrations of **MPD1** and **MPD2**. This result shows a trend involving an increase in the concentration of metal complexes with the rate of the NBT reaction, with the increasing formation of the superoxide radical varying as there is an increase up to the highest concentration of metal complexes (60 μmol L^{-1}).

One additional measurement was carried out to further validate the production of this radical which used the superoxide dismutase (SOD) enzyme. This enzyme catalyzes the dismutation of the superoxide radical into H_2O_2 and O_2. SOD is one of the most important enzymes that acts as a cellular antioxidant system, which is found in the cytoplasm and mitochondria of mammalian cells.[64] These experiments were performed under the same conditions as before but with the addition of SOD into the reaction mixture, and no spectroscopic changes were noticed (Fig. S13, ESI†). These results reinforced that the radical generated was the superoxide ion. We proposed that the formation of $O_2^{\bullet-}$ occurs during the ruthenium redox process according to a catalytic cycle (Fig. S14, ESI†) in analogy to other systems. These results support the photoproduction of superoxide ions in a redox process involving the ruthenium compounds, as shown in Fig. 5. These results highlights that reduced glutathione[65] is a key factor promoting the sustained generation of this specific reactive oxygen species (ROS). Altogether, these results indicate that **MPD1** and **MPD2** have a significant capacity to photogenerate superoxide, which, along with singlet oxygen, may be suitable agents for causing cell death. This may lead to controlled damage to biomolecules such as DNA, promoting possibly bactericidal effects as further described for **MPD1** and **MPD2**.

Interaction and damage to DNA

Once these metal complexes exhibited thermal and photochemical stability and were capable of photogenerating ROSs, we looked at their ability to interact and eventually damage important biological targets such as DNA. A DNA titration monitored by electronic absorption in the UV–vis range was carried out, but even after the addition of 60 μmol L^{-1} DNA (*calf thymus* DNA, ct-DNA) into the metal complexes (at 10 μmol L^{-1}), no significant spectroscopic changes were observed (Fig. S15, ESI†). The lack of changes could be due to weak (or none) interactions or even other types of interactions with minor structural disturbances not well reported by UV-vis spec-

troscopy. Based on this, we decided to look further at this issue using a more sensitive structural technique such as circular dichroism (CD) spectroscopy.

Thus, an attempt to investigate the binding of these metal complexes to double stranded *calf thymus* DNA (ct-DNA) and *salmon* DNA (s-DNA) was made using CD. For this purpose, **MPD1** or **MPD2** was mixed with DNA at different ratios and also pre-incubated for 1 h at 25 °C. Circular dichroism spectra of these samples were recorded as shown in Fig. 6. It is important to mention that the measured CD spectra from 220 to 350 nm were indicative of the retention of the B-DNA conformation in both types of DNAs. In addition to the positive CD signal centered at 265 nm, there was also a negative band at 245 nm. The incremental addition of ruthenium complexes to both ct-DNA and s-DNA resulted in a significant reduction in ellipticity for each one of these CD bands.

There is a clear effect of the metal compounds on DNA, which was not seen before by electronic spectroscopy, where both ruthenium complexes induced reductions in the ellipticity of the double stranded DNA (Fig. 6). These results suggest that both molecules have likely similar interactions with DNA as we would expect based on their structural similarity. As shown in Fig. 6, the CD spectrum undergoes changes in both positive and negative bands upon incubation with the metal complexes. They promoted a reduction in the intensity of these bands suggesting a likely interaction between the metal complex and DNA. In addition, **MPD1** also showed a drastic change in the spectra of the two investigated DNAs, exhibiting in both cases a characteristic positive peak at 262 nm and a negative peak at around 298 nm.[66] This profile indicates a likely transition from B-DNA to Z-DNA forms.[67] For **MPD2**, there was a decrease in the intensity of the bands with moderate similarity to that seen with **MPD1**. These spectral changes suggest disruption of the B-DNA secondary structure, impacting nucleobase stacking and the local helix geometry.[68] The reduction in elliptic intensity at the 271 nm band following

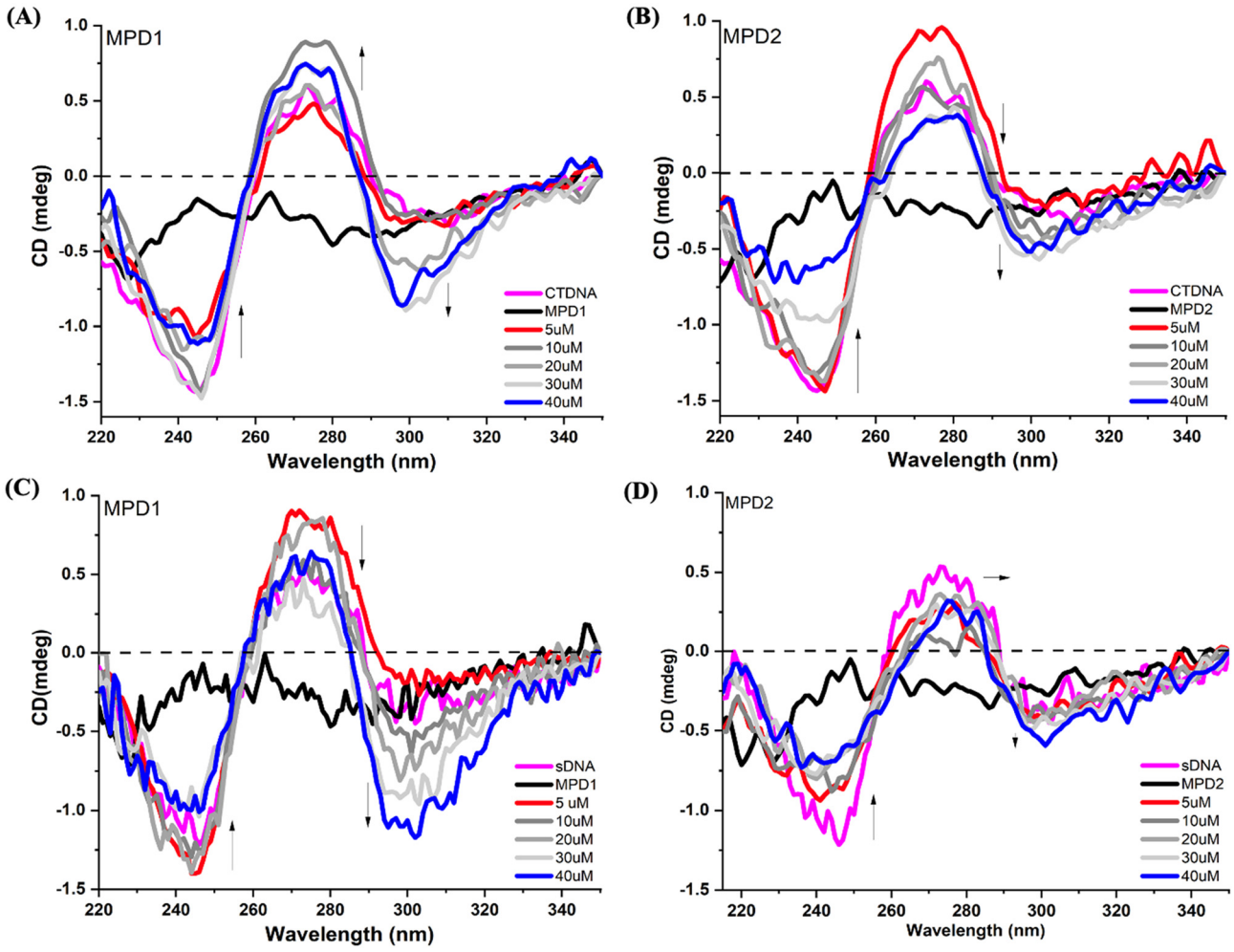

Fig. 6 DNA binding studies monitored by circular dichroism. Spectra of 100 μmol L^{-1} bovine calf thymus DNA (ct-DNA, top) and salmon DNA (s-DNA, bottom) incubated for 1 h with increasing concentrations of **MPD1** (A and C) and **MPD2** (B and D) ruthenium(III) complexes. The concentrations of the ruthenium complexes are ranging from 5 to 40 μmol L^{-1}. The solid magenta line represents only ct-DNA and s-DNA, while the black lines are the metal complexes alone in the maximum concentration employed. Arrows indicate a trend upon increasing the concentration of the ruthenium complex.

compound interaction supports an increase in the winding angle and a decrease in the helix twist. This intensity reduction may also indicate a conformational shift in the DNA duplex, possibly altering the base pair count per helical turn, as observed in the transition from B-form DNA (10.4 bp per turn) to C-form DNA (9.4 bp per turn).[69] Accordingly, we suggest that the interaction of **MPD2** with DNA reduces right-handed helicity, modifying base stacking and inducing an intermediate state with characteristics of the C-DNA form, but further studies need to be done to better describe this process.[69] Nonetheless, even modest structural changes in a metal compound can affect its capacity to interact and disturb specific regions of the DNA.

Cleavage of DNA. Once we noticed that these metal complexes could eventually interact with DNA, most likely through a non-covalent mode, we investigated their ability to damage DNA, particularly upon light stimulation. This study was carried out using agarose gel electrophoresis, in which pUC19 DNA (20 μmol L^{-1}, in base pairs) was mixed with metal complexes (5, 10, 20, 30, and 60 μmol L^{-1}) and exposed or not exposed to blue light for 1 h. In addition to these conditions, we also included GSH (5 mmol L^{-1}), given the ability of the metal complexes to generate superoxide radicals, as shown in our previous experiments. Oxidative cleavage of DNA usually requires a stimulus such as light, and oxidizing or reducing agents to initiate the process. This event can damage the sugar and nitrogenous base of the DNA or both, which results in the formation of DNA fragments that cannot be reconnected.[70]

Our results showed that **MPD1** and **MPD2** are indeed efficient DNA damaging agents when exposed to blue light, but there is also some effect even in the dark (Fig. 7). In fact, the formation of nicked DNA (form II) was observed using *ca.* 5 μmol L^{-1} metal complex, and by increasing the concentration of the compounds it is possible to observe that there is also greater damage to the DNA. The more pronounced disappearance of DNA after blue light irradiation suggests a significant degradation, which was subsequently investigated by size exclusion chromatography as described below. In addition, the mobility of the remaining DNA is reduced, especially after light irradiation. An additional test was performed with the addition of GSH (Fig. S16, ESI†), where there was no apparent influence of GSH on the photodegradation process, which may indicate that DNA degradation is likely not based on superoxide radical production. These metal compounds continued their cleavage activity without any further significant enhancement. Indeed, reduced glutathione seems

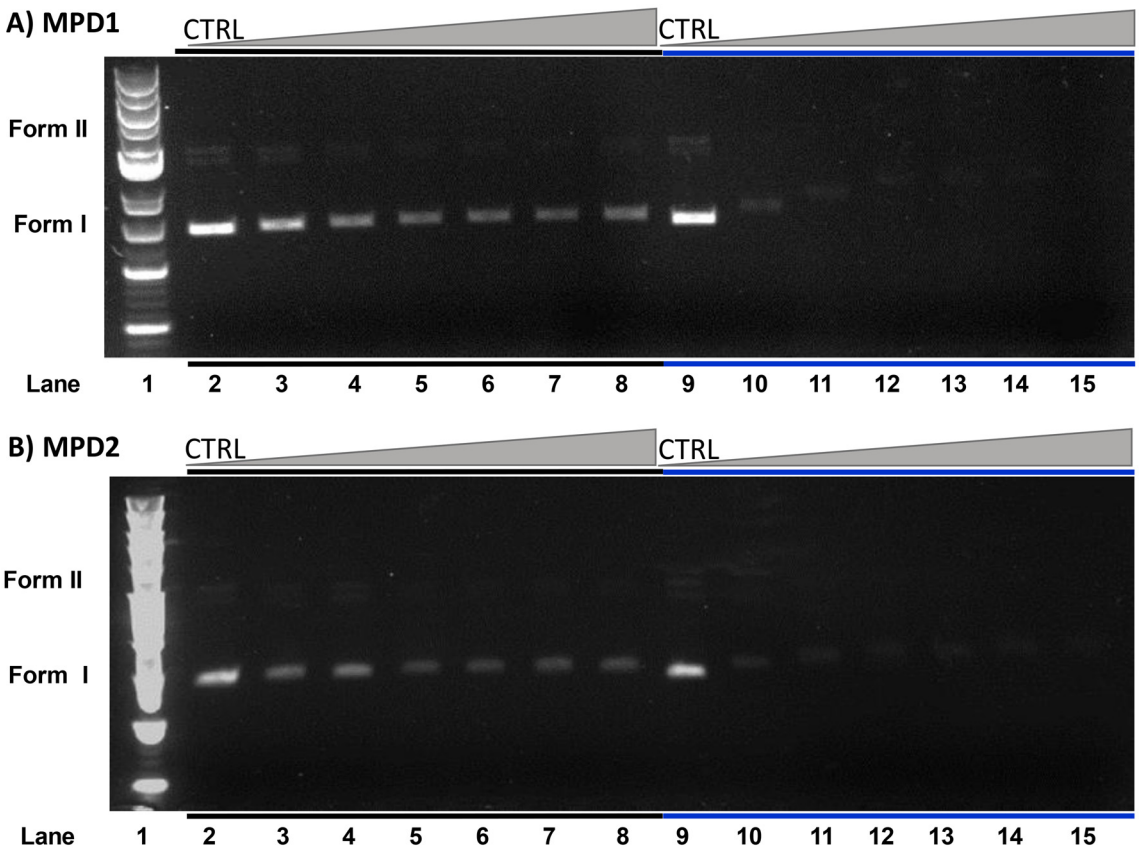

Fig. 7 DNA cleavage studies. pUC19 DNA (20 μmol L^{-1}, in base pairs) used with **MPD1** (A) and **MPD2** (B) with and without 1 h of blue light irradiation. In all experiments, lane 1 contains only the linear DNA ladder, lanes 2 and 9 have only pUC19 DNA, while lanes 3–8 and 10–15 contained DNA along with the concentrations of 5, 10, 20, 30, 40 and 60 μmol L^{-1} of the **MPD1** (A) and **MPD2** (B) complexes. The dark and blue boxes indicate that the experiment was carried out without or with blue light irradiation, respectively.

to moderately reduce damage, which could be due to the consumption of the photogenerated singlet oxygen species, a much stronger DNA cleavaging agent. Based on this, we have confirmed their ability to photogenerate ROSs leading to DNA cleavage likely *via* oxidative pathways.

Aiming to shed some light on this process, we used size-exclusion-based spin columns (Bio-spin Bio-gel P30, Bio-Rad) as a strategy to investigate the integrity of the DNA. These highly efficient spin columns are based on a polyacrylamide resin able to exclude compounds based on their molecular weight. In this column, only large molecules (>20 base-pair nucleotides or globular proteins of MW > 40 000 Da) can be excluded from entering into the porous stationary phase and be trapped. Thus, a large size DNA is fully excluded and promptly collected after centrifugation, while the metal complex or any other small molecule is trapped in the gel. However, if there is a significantly strong interaction of a small molecule with DNA, then, this species might be carried along and removed from the column. In our case, if the metal complexes are in this collected sample, then, we could identify them by detecting their absorption bands in the visible range.

In this study, we mixed salmon DNA (MW > 2000 base pairs) with an excess of the metal complexes (MW < 800 Da) in 10 mmol L^{-1} Tris buffer, pH 7.4, and then they were incubated for 1 h or 4 h in the dark. Additionally, another sample was irradiated with blue light for 1 h. Two controls of only DNA or metal complexes were also employed. These samples were applied onto the bio-spin column and excluded samples were collected, which were subjected to measurement by electronic spectroscopy.

Notably, two features were seen in these samples. First of all, some collected samples containing DNA and the metal complexes together showed bands in the visible range of the electronic spectra confirming the presence of the metal complexes (Fig. S17, ESI†). Besides that, there was a significant decrease in the absorption band at *ca.* 255 nm, which is mainly associated with DNA. It is important to mention that the collected sample from the metal complex alone when applied onto the bio-spin column did not show any absorption bands in the visible range, while free salmon DNA alone had its maximum absorption band recorded as a reference. Based on this, there is further evidence that **MPD1** binds to DNA (at least with a fraction and in large excess), which allowed this compound to be collected in the excluded sample along with this macromolecule (Fig. 8 and Fig. S17, ESI†). Interestingly, the sample irradiated with blue light showed an even stronger increase in the amount of the metal complex carried with DNA (*ca.* 6.1 μmol L^{-1}). This result suggests that **MPD1** can bind to DNA, which might be as strong as through covalent interactions. In addition to this, by monitoring the characteristic band of DNA, at *ca.* 255 nm, we can estimate a relative decrease in the DNA concentration of *ca.* 31–42% (from 1–4 h),

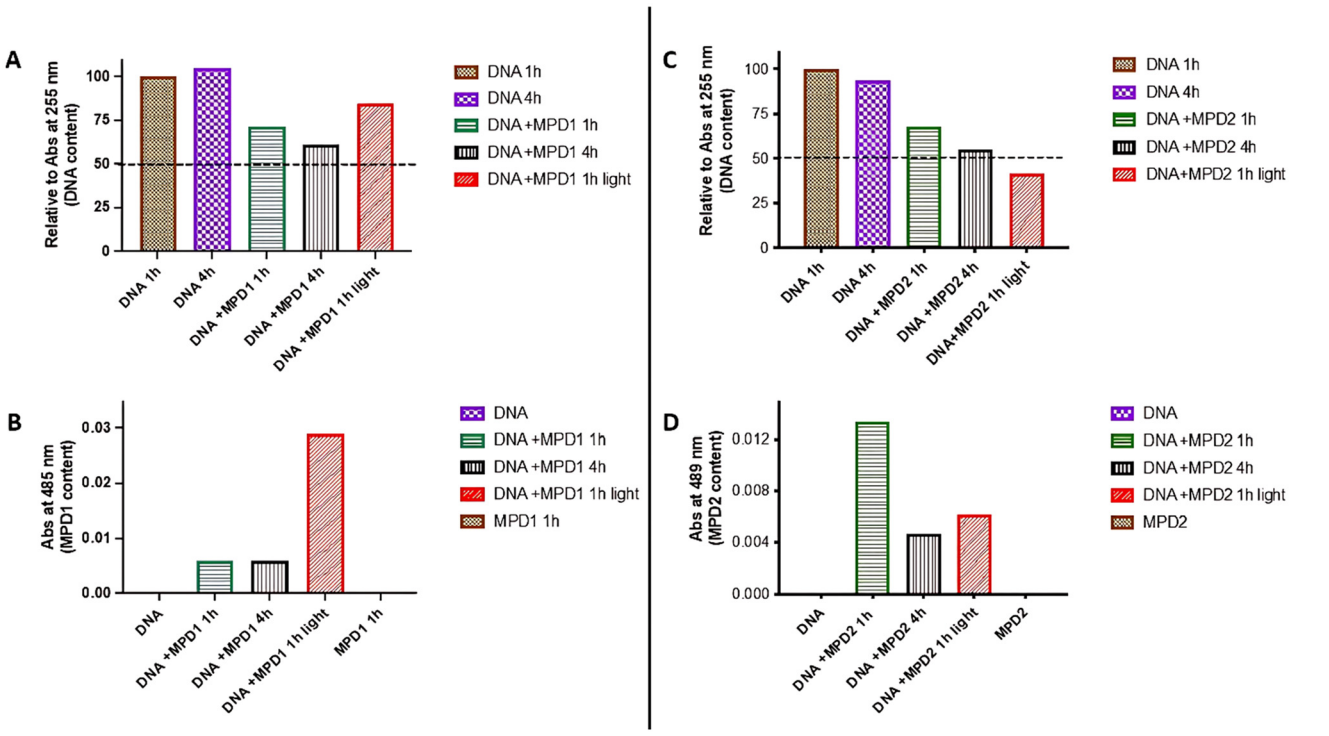

Fig. 8 Investigation of binding and degradation of salmon DNA (100 μmol L^{-1}) promoted by the metal complexes (at 200 μmol L^{-1}) in 100 mmol L^{-1} Tris buffer of pH 7.4 at 25 °C using size-exclusion bio-spin columns. Panel (A) shows the effect of **MPD1** in the relative amount of DNA, based on the band at 255 nm, while panel (B) shows the absorbance measured in the visible range for this sample. Panel (C) shows the effect of **MPD2** in the relative amount of DNA, based on the band at 255 nm, while panel (D) shows the absorbance measured in the visible range for this sample (panel A relative amount of DNA based on the 255 nm band).

indicating that **MPD1** can also degrade DNA even without light. There is an increase in this DNA band after light irradiation, but it can be attributed to the contribution of the intraligand band of the metal complex associated with it. Indeed, if this contribution is taken into consideration, we can estimate a further decrease in DNA. These results indicate that at least a fraction of **MPD1** can strongly bind to DNA, but it can also promote the direct degradation of DNA as well. These results are in agreement with previous studies, where agarose gel electrophoresis indicated the disappearance of DNA even without light irradiation and CD measurements showed significant changes in both bands of DNA.[71]

We noticed some distinct behavior when using **MPD2** in this assay. There was a slightly faster and consistent decrease in the DNA concentration, where *ca*. 29% and 40% were degraded after 1 h and 4 h of incubation in the dark, respectively. This degradation was significantly enhanced upon blue light irradiation achieving *ca*. of 55% of DNA degradation within 1 h, almost double of what was seen in the dark (Fig. 8). We still observed the metal complex eluted along with DNA, but it was expressively much more with **MPD1** (with blue light irradiation), which was not similar for **MPD2**. Our estimated concentration of **MPD2** linked to DNA was 2.2 μmol L^{-1} in the dark and even lower in the light irradiated sample (1.09 μmol L^{-1}). These results showed that light irradiation can better contribute to DNA degradation promoted by **MPD2**, even though it binds less, while in the dark this effect is lower and only moderate degradation is observed. In this case, more **MPD1** can remain attached and carried through the resin. In summary, these results supported **MPD2** as a more efficient compound to degrade DNA upon light irradiation than **MPD1**, which agrees with our electrophoresis results.

Antibacterial activity

These metal complexes were investigated as potential antimicrobial agents against six bacterial strains (Gram-positive and Gram-negative), where we also used blue or red-light irradiation. Gram-positive bacterial strains (*e.g.*, *Staphylococcus aureus* and *Staphylococcus epidermidis*) were much more sensitive to these metal complexes. Actually, the lack of activity for Gram-negative bacteria is more commonly reported, considering the nature of their bacterial cell wall, which is relatively more complex with an additional cell membrane[72,73] making it harder for uptake.

Antimicrobial activities against bacteria are summarized in Table 4 and S6, ESI;† some microorganisms had minimum inhibitory concentrations (MICs) and minimum bactericidal concentrations (MBCs) ranging from 4.0 up to 259.6 μmol L^{-1}. Interestingly, **MPD2** was the only one showing MIC and MBC activity against Gram-negative bacteria even without light irradiation, but still at a significantly high concentration (128.4 μmol L^{-1}). It is important to mention that this result was usually enhanced upon blue or red-light irradiation.

We noticed that **MPD1** and **MPD2** exhibited moderate antimicrobial activity in the dark, while upon blue or red-light irradiation there was an expressive enhancement in these

Table 4 Antimicrobial assay using **MPD1** and **MPD2**

Metal complex	Blue LED		*S. aureus* ATCC 25923 μg mL^{-1} (μmol L^{-1})	*S. aureus* ATCC 700698 μg mL^{-1} (μmol L^{-1})	*S. epidermidis* ATCC 12228 μg mL^{-1} (μmol L^{-1})	*S. epidermidis* ATCC 35984 μg mL^{-1} (μmol L^{-1})
MPD1	On	MIC[a]	3.9 (4.06)	15.6 (16.24)	7.8 (8.12)	3.9 (4.06)
		MBC[b]	7.8 (8.12)	31.2 (32.4)	7.8 (8.12)	7.8 (8.12)
	Off	MIC	62.5 (64.9)	125.0 (130.1)	62.5 (64.9)	62.5 (64.9)
		MBC	62.5 (64.9)	ND	62.5 (64.9)	62.5 (64.9)
MPD2	On	MIC	3.9 (4.0)	15.6 (16.0)	3.9 (4.0)	3.9 (4.0)
		MBC	3.9 (4.0)	31.2 (32.0)	7.8 (8.0)	7.8 (8.0)
	Off	MIC	31.2 (32.0)	62.5 (64.12)	31.2 (32.0)	31.2 (32.0)
		MBC	125.0 (128.24)	ND	31.2 (32.0)	250.0 (256.48)
Metal complex	Red LED		*S. aureus* ATCC 25923 μg mL^{-1} (μmol L^{-1})	*S. aureus* ATCC 700698 μg mL^{-1} (μmol L^{-1})	*S. epidermidis* ATCC 12228 μg mL^{-1} (μmol L^{-1})	*S. epidermidis* ATCC 35984 μg mL^{-1} (μmol L^{-1})
MPD1	On	MIC	31.2 (32.4)	250.0 (259.6)	15.6 (16.0)	31.2 (32.4)
		MBC	31.2 (32.4)	ND	62.5 (64.9)	62.5 (64.9)
	Off	MIC	62.5 (64.9)	125.0 (129.8)	62.5 (64.9)	62.5 (64.9)
		MBC	62.5 (64.9)	ND	62.5 (64.9)	62.5 (64.9)
MPD2	On	MIC	15.6 (16.0)	62.5 (64.12)	15.6 (16.0)	31.2 (32.0)
		MBC	15.6 (16.0)	250.0 (256.48)	31.2 (32.0)	125.0 (128.4)
	Off	MIC	31.2 (32.0)	62.5 (64.12)	31.2 (32.0)	31.2 (32.0)
		MBC	125.0 (128.4)	ND	31.2 (32.0)	250.0 (256.48)

[a] Minimum inhibitory concentration. [b] Minimum bactericidal activity. MIC and MBC reported in μg mL^{-1} (or μmol L^{-1}). (ND) not detected even at the highest concentration of 250 μg mL^{-1}.

Table 5 *In vitro* cytotoxicity (IC_{50}, μmol L^{-1}) results against MDA-MB-231, A2780, and A549 cancer cells and non-cancerous MRC-5 cells in the dark (48 h and 72 h of incubation) and upon light irradiation (460 nm, 10 min, 18 mW cm^{-2}, 10.8 J cm^{-2}, and 48 h of incubation). Data are presented as mean ± SD of three independent replicates. PI = IC_{50}(tumor $cell_{dark}$)/IC_{50}(tumor $cell_{light}$). nd = not determined even at the highest concentration used

Cytotoxicity, IC_{50} (μmol L^{-1})												
	MDA-MB-231			A2780			A549			MRC-5		
	Dark	Light	PI	Dark	Light	PI	Dark	Light	PI	Dark	Light	PI
MPD1	>50	>50	—	>50	10.62 ± 1.10	>4.7	>50	>50	—	>50	nd	—
MPD2	>50	>50	—	>50	>50	—	>50	>50	—	>50	nd	—

activities. The photoactivity index (PI) was calculated as the ratio of the biological activity in the dark and upon light irradiation indicating the degree of improvement of the biological activity after photoirradiation. These antibacterial assays showed a significant increase in MIC after irradiation (photoactivity index, PI, of 16 to >32 times), with reasonably low MICs of 16.0 μmol L^{-1} (*S. aureus*, ATCC 700698) and 4.0 μmol L^{-1} (*S. epidermidis* ATCC 35984) for both metal complexes after blue light irradiation. Interestingly, a MIC of 16.0 μmol L^{-1} was also observed for *S. epidermidis* ATCC 12228 after irradiation with red light using **MPD1** and **MPD2**. Such results with red light are quite encouraging considering its deeper penetration into the skin and use in photodynamic therapy.

Notably, promising results were collected also for a biofilm-forming strain *S. epidermidis* (ATCC 35984), which has been directly associated with an apparent decrease in the efficacy of antibiotics.[62] **MPD1** showed activity even in the dark, with MIC values enhanced 8- and 16-fold when irradiated with red or blue light, respectively. There were also promising results for **MPD2** with MIC values against the *S. aureus* strain (ATCC 25923) of 32.0 μmol L^{-1} in the dark, which was enhanced 2- and 8-fold upon red or blue light irradiation, respectively. Remarkably, the MBC improved even more by 8- and 32-fold upon red and blue light irradiation, demonstrating the strong photoactivity of this compound as well. *Staphylococcus aureus* strains have had about 29% of isolates resistant to methicillin, according to the data available in 2008, while this percentage increased to 47% by 2014, indicating a difficult current scenario.[74] There is a clear need for new and more effective agents against *Staphylococcus aureus* in the face of resistance. It is also suggested that the promising antibacterial activity of these compounds could be explained by the fact that they generate ROSs enabling the elimination of bacterial strains.

Cytotoxic activity

In addition to bacteria, the cytotoxic activities of **MPD1** and **MPD2** were evaluated in human tumor cell lines MDA-MB-231 (human triple-negative breast adenocarcinoma of mesenchymal phenotype), A549 (human lung alveolar epithelial basal cell adenocarcinoma), A2780 (human ovarian adenocarcinoma) and MRC-5 health cells (human lung cells) by the MTT colorimetric assay. Notably, **MPD1** and **MPD2** showed no significant cytotoxicity (IC_{50} > 50 μmol L^{-1}) under these conditions after 48 h and 72 h of incubation. On the other hand, **MPD1** had its cytotoxicity increased in A2780 cells after light irradiation. A moderate phototoxicity index (PI) was observed for this compound, revealing its enhanced potency (4.7-fold) upon blue light irradiation (Table 5).

Ruthenium(II) complexes with phenyl-terpyridine ligands have been investigated as potential anticancer agents having other structural ligand vicinities.[67,68] A series of these compounds showed antitumor activity against various cell lines with an IC_{50} value of 58.9 μmol L^{-1} ± 4.7 for MCF-7 cells and 73.3 μmol L^{-1} ± 5.4 for A549 cells with an SI value of 3.16.[75] Nonetheless, it is noteworthy that both of our compounds seemed to exhibit a safe profile for potential use as antibiotic agents.

Conclusions

Our data were consistent with the formulation of the two proposed ruthenium compounds. Besides that, these compounds showed the capacity to photogenerate a series of ROSs, including superoxide ions. Singlet oxygen was photogenerated with close quantum yield values of 0.13 and 0.17 for **MPD1** and **MPD2**, in methanol, respectively. Interestingly, **MPD2** was also able to photogenerate hydroxyl radicals. These compounds exhibited a hydrophilic behavior with negative log *P* values maybe causing their lack of cytotoxicity against mammalian cells. DNA binding and efficient damage were measured which may be influencing antibiotic activity suggesting **MPD2** as a better option. Actually, antibacterial assays showed great activity against Gram-positive bacteria upon blue (MIC and MBC up to 4 μmol L^{-1}) and excitingly with red-light irradiation (MIC and MBC up to 16 μmol L^{-1}). This enhancement upon light irradiation can be explained by their strong absorption in the visible region even with a slight shift towards the red region. Altogether, these compounds have shown promising antibiotic action even upon red light irradiation opening further opportunities for investigations.

Experimental section

Chemicals

Acetonitrile, tetra-*N*-butylammonium perchlorate (PTBA), 2-acetylpyridine, potassium bromide (KBr), *p*-tolualdehyde,

benzaldehyde, and ammonium hexafluorophosphate were purchased from Sigma-Merck, and ruthenium(III) chloride was obtained from Precious Metals Online (Australia). Diethyl ether, dimethylsulfoxide, sodium hydroxide, and potassium hydroxide were purchased from Synth, while ethanol, acetone, methanol, dichloromethane, acetonitrile, ammonium acetate, and chloroform were obtained from Biograde.

Biological assays employed Tryptic Soy Agar (TSA) purchased from Liofilchem (Italy), Mueller-Hinton Broth (MHB), Phosphate Buffered Saline (PBS; pH 7.4), and Crystal Violet (CV) for the assay of different bacterial strains. Dulbecco's Modified Eagle's Medium (DMEM), bovine fetal serum (FBS), Roswell Park Memorial Institute 1640 (RPMI 1640) medium (all were purchased from GE-Hyclone®) and 3-(4,5-dimethylthiazol-2-yl)-2,5-diphenyltetrazolium bromide (MTT) were used to determine the cytotoxic activity.

Physical measurements

All measurements of the electronic spectra were done with a Cary 5000 UV–vis-NIR (Agilent), using a quartz cuvette of 1 cm path length. Fluorescence spectroscopy was performed using a Quanta-Master QM-40 (PTI) with a quartz cuvette. NMR spectra were recorded in deuterated solvents as described in the text using a BRUKER 300 MHz NMR spectrometer. Electrochemical measurements were done using an Epsilon potentiostat (Bioanalytical Systems Inc. (BAS)) E2 818 using a single-compartment glass cell filled with inert atmosphere (argon)-purged acetonitrile containing a tetra-*N*-butylammonium perchlorate (0.1 mol L^{-1}) electrolyte solution and equipped with glassy-carbon working, platinum-wire auxiliary, and Ag/AgCl pseudo-reference electrodes, at 25 ± 0.2 °C. All potentials described in this study were reported *versus* Ag/AgCl electrode, which, under the given experimental conditions, gave a value of 0.410 V for the ferrocene/ferrocenium couple.[76] High-resolution mass spectral data were recorded using an Agilent 6545 Q-TOF MS (Agilent Technologies, Santa Clara, CA, USA), where qualitative analysis of the samples was carried out using a system equipped with a jet electrospray interface (ESI) in the positive mode (ESI+), using the following parameters for ionization: a gas temperature of 350 °C; a gas flow of 10 L min^{-1}; a nebulizer pressure of 40 psi; a sheath gas temperature of 325 °C; a sheath gas flow rate of 9 L min^{-1}; and a voltage of 550 V. The metal complexes were analyzed by direct infusion, having a composition of the mobile phase of 5% H_2O (solvent A, 0.1% formic acid) and 95% ACN (solvent B with 0.1% formic acid). This mobile phase flow rate was 0.300 mL min^{-1} and the injection volume was 3 μL. Data were recorded in full MS scan using a range of *m*/*z* 50 to 1500 *m*/*z*, while data were processed using Mass Hunter Workstation Software version B.08.00.

Syntheses

All chelating ligands were prepared as described in the literature.

The 4′-phenyl-2,2′:6′,2″-terpyridine (phtpyH) ligand was prepared and characterized as reported elsewhere.[77] Yield: 6.45 g (69%), ^{1}H NMR 500 MHz, ($CDCl_3$): δ 8.53 (m, 4H), 8.46 (dt, 2H), 7.70 (m, 2H), 7.67 (m, 2H), 7.30 (td, 2H), 7.25 (m, 1H), 7.14 (m, 2H). IR: ν(C═C) 1600 cm^{-1}. Elemental analysis for $C_{21}H_{15}N_3 \cdot H_2O$: calc. (exp.)%: C, 81.53 (80.84); H, 4.89 (4.77); N, 13.58 (13.31).

The 4′-(*p*-tolyl)-2,2′:6′,2″-terpyridine (phtpyMe) ligand was prepared and characterized as reported elsewhere.[77] Yield: 1.41 g (43%), ^{1}H NMR 500 MHz, ($CDCl_3$): δ 8.61 (m, 4H), 8.54 (d, 2H), 7.73 (m, 4H), 7.21 (m, 4H), 2.31 (s, 3H). IR: ν(C═C) 1585 cm^{-1}. Elemental analysis for $C_{22}H_{17}N_3 \cdot H_2O$: calc. (exp.)%: C, 77.63 (65.89); H, 5.33 (5.59); N, 12.34 (12.43).

The 4,5-diazafluoren-9-one (DFO) ligand was prepared and characterized as reported elsewhere.[78] Yield: 1.48 g (43%), ^{1}H NMR 500 MHz, ($CDCl_3$): δ 8.80 (dt, 2H), 8.09 (dd, 2H), 7.51 (ddd, 2H). IR: ν(C═O) 1722 cm^{-1}. Elemental analysis for $C_{11}H_6N_2 \cdot H_2O$: calc. (exp.)%: C, 66.00 (65.89); H, 4.02 (3.49); N, 13.95 (13.99).

The precursor metal complexes with the formulation [Ru(phtpy-R)(DMSO)(Cl_2)] (where R = H or Me = $-CH_3$) were synthesized following a similar procedure described for [Ru(tpy)(DMSO)Cl_2].[79]

[Ru(phtpyH)(DFO)(Cl)](PF_6) (MPD1) or [Ru(phtpyMe)(DFO)(Cl)](PF_6) (MPD2)

A suspension of [Ru(phtpy-R)(DMSO)Cl_2] (100.0 mg, 0.174 mmol) and 4,5-diazafluoren-9-one (50.0 mg, 0.274 mmol) in ethanol (30 mL) was heated and then kept under reflux and an argon atmosphere for 18 h. After that, the resulting mixture was rotary evaporated under vacuum to *ca.* 5 mL, and NH_4PF_6 was added to the remaining mixture. Then, a dark red solid was collected by filtration and washed with diethyl ether.

MPD1: Yield: 121 mg (70.9%), ^{1}H NMR (Fig. S1 of the ESI,† 500 MHz, $(CD_3)_2SO$): δ 9.42 (d, 1H, 11*), 9.16 (s, 2H, 4), 8.94 (d, 2H, 5), 8.45 (d, 1H, 9*), 8.32 (d, 2H, 8), 8.11 (d, 1H, 10*), 8.06 (m, 4H, 3 and 6), 7.94 (d, 1H, 11), 7.72 (t, 2H, 7), 7.62 (s, 1H, 1), 7.54 (d, 1H, 9), 7.48 (d, 2H, 2), 7.18 (t, 1H, 10). IR: ν(C═O) 1737 cm^{-1}. $C_{32}H_{21}ClN_5ORuPF_6$. Elemental analysis: calc. (exp)%: C, 49.72 (49.43); H, 2.74 (2.84); N, 9.06 (9.46). Conductivity measured in acetonitrile (1 mmol L^{-1}) is 138.7 Ω^{-1} cm^2 mol^{-1} (1 : 1). HR-MS: 628.0497 u (theoretical 628.0473 u, $[M + H - PF_6]^+$).

MPD2: Yield: 55 mg (34.1%), ^{1}H NMR (Fig. S3 of the ESI,† 300 MHz, $(CD_3)_2SO$): δ 9.42 (d, 1H, 11*), 9.12 (s, 2H, 4), 8.92 (d, 2H, 5), 8.43 (d, 1H, 9*), 8.23 (d, 2H, 8), 8.10 (d, 1H, 10*), 8.04 (m, 4H, 3 and 6), 7.92 (d, 1H, 11), 7.52 (m, 3H, 7 and 9), 7.47 (t, 2H, 2), 7.17 (t, 1H, 10), 2.48 (s, 3H, 1). IR: ν(C═O) 1737 cm^{-1}. $C_{33}H_{23}ClN_5ORuPF_6$. Elemental analysis: calc. (exp)%: C, 48.16 (47.61); H, 3.31 (3.47); N, 8.51 (8.11). Conductivity measured in acetonitrile (1 mmol L^{-1}) is 161.6 Ω^{-1} cm^2 mol^{-1} (1 : 1). HR-MS: 642.0628 u (theoretical 642.0629 u, $[M + H - PF_6]^+$).

X-ray crystal structure determination

Single-crystal X-ray structure determination. Single crystals of **MPD1** and **MPD2** were obtained through the process of slow

evaporation, where the compound was dissolved in acetone, placed in a flask containing ethyl ether and left to evaporate at room temperature. Single crystal X-ray diffraction data (ϕ scans and ω scans with κ and θ offsets) were collected using a Bruker D8 Venture κ-geometry diffractometer equipped with a Photon II CPAD detector and an IμS 3.0 Incoatec Mo Kα (λ = 0.71073 Å) microfocus source. A suitable crystal for the compound was chosen and mounted on a Kapton fiber with a MiTeGen MicroMount using immersion oil. The crystals were kept at 300 K (**MPD1**) and 150 K (**MPD2**) for data collection using an Oxford Cryostream system (800 series Cryostream Plus) attached to the diffractometer. APEX 4 software was used for unit cell determination and data collection.[80,81] The data reduction and global cell refinement were made using the Bruker SAINT+ software package,[76] and a multi-scan absorption correction was performed using SADABS.[82] Using the Olex2[83] interface program in the SHELX suite, the structure was solved by the intrinsic phasing method implemented in ShelXT,[84] allowing the location of most of the non-hydrogen atoms. The remaining non-hydrogen atoms were located from difference Fourier maps calculated from successive full-matrix least-squares refinement cycles on F^2 with ShelXL[85] and refined using anisotropic displacement parameters. In **MPD2**, residual electron densities were observed in solvent-accessible voids and associated with disordered solvent molecules and treated with the PLATON/SQUEEZE program.[86] The programs Mercury[87] and Platon[88] were used to prepare the artwork representations for publication. Hydrogen atoms were placed according to geometrical criteria and treated using the riding model. The accession numbers for the crystallographic data reported in this paper are CCDC 2375481 and 2375482.†

DFT calculations. The geometry of all metal complexes was optimized at the density functional theory (DFT) level. Calculations were executed using the Gaussian 09 program package, Revision A.02 (Gaussian, Inc., Wallingford, CT, USA)[89] with the B3LYP functional.[90–92] The LANL2DZ relativistic effective core potential basis set[93,94] was used for the Ru atom and the 6-311G(d,p) basis set[95] was used for the lighter atoms (C, N, O, Cl, and H). The absence of imaginary frequencies in vibrational analysis calculations confirmed that all optimized structures were in minimum potential energy. The TD-DFT (time-dependent density functional theory) approach was employed to investigate the electronic properties of the metal complexes. The UV–Vis spectra of all compounds were simulated in water, using the polarizable continuum model (PCM).[96] Molecular orbital composition, UV–vis spectra and assignment of electronic transitions were extracted from output files using Multiwfn[97] and GaussSum 3.0[98] software.

Measurement of reactive oxygen species (ROSs)

Singlet oxygen measurement. The reaction of $^1O_2$ with 1,3-diphenylisobenzofuran (DPBF) was employed to measure the singlet oxygen quantum yield as monitored using fluorescence.[99] In all studies, we used a quartz fluorescence cuvette containing 2.5 mL of methanol and acetonitrile with DPBF (20 μmol L^{-1}) and **MPD1** or **MPD2** (20 μmol L^{-1}) or a standard singlet oxygen photogenerator ($[Ru(bpy)_3]^{2+}$ or methylene blue (10 μmol L^{-1})). This cuvette was irradiated with a blue (λ_{max} 463 nm) (t_{irrad} 5.0 s) or red (λ_{max} 631 nm) (t_{irrad} 120.0 s) LED (all light sources from Basetech Conrand, 20 W) and placed back in the fluorimeter for measurement of the remaining fluorescence of DPBF ($\lambda_{excitation}$ = 410 nm, $\lambda_{max.\ emission}$ = 479 nm). The consumption of DPBF was measured by the decrease in its fluorescence at 479 nm. The quantum yield of the singlet oxygen produced (Φ_Δ) by $[Ru(bpy)_3]^{2+}$ (Φ_Δ = 0.84) and methylene blue (Φ_Δ = 0.64), in air-saturated acetonitrile solution, was taken as references for blue and red-light sources, respectively. These quantum yields were determined according to the literature,[100] and the singlet oxygen quantum yield was determined using the equation below:

$$\frac{k_s}{k_{rc}} = \frac{\Phi_\Delta(\text{sample}) - \delta}{\Phi_\Delta(\text{standard}) - \delta}$$

where k_s and k_{rc} are obtained from the slope of the kinetic curves of $\ln(I/I_0)$ *versus* time of light irradiation of the sample and the reference compound. I and I_0 are the intensities of the maximum emission of DPBF at various times and at time zero, respectively. Since DPBF undergoes some spontaneous photodegradation upon light irradiation in the blue region or more energetic regions,[101] this effect was corrected by adding the δ factor, which is the angular coefficient of the kinetic curve of the DPBF compound in the absence of photosensitizer compounds.

In addition, Singlet Oxygen Sensor Green (SOSG, Thermo Fisher Scientific) (λ_{exc} = 490 nm) was used as a highly selective probe, also in aqueous media. All measurements were performed in methanol as the preferred solvent and also in water, although the latter suppresses probe luminescence upon reaction with $^1O_2$, whereas acetonitrile has been shown to accelerate photodissociation.[59] The increase in the emission band at 528 nm was monitored and used for calculations. A quartz cuvette containing 1000 μL of the metal complexes (10 μmol L^{-1}) or a standard singlet oxygen photogenerator ($[Ru(bpy)_3]^{2+}$) (10 μmol L^{-1}) in methanol was irradiated with a blue LED (at 463 nm, 20 W) ($time_{irrad}$ 5.0 s) in the presence of SOSG (1 μmol L^{-1}). Additionally, a cuvette containing only SOSG in methanol was exposed to light, and its emission spectra were monitored as a negative control. Plots of emission intensity changes *versus* time of light exposure were fitted to a linear regression and the slope was calculated. The singlet oxygen quantum yield (Φ_Δ) of the $[Ru(bpy)_3]^{2+}$ complex in methanol, previously reported as 0.87,[102] was used as a reference for our relative quantum yield measurements. The quantum yield of singlet oxygen was determined using the same equation as previously described for DPBF.

Hydroxyl radical measurement. Aminophenyl fluorescein (APF, Thermo Fisher Scientific) was used to measure the photogeneration of the hydroxyl radical ($HO^\bullet$) by monitoring the increase in the emission band at 515 nm. A quartz cuvette containing 1000 μL of the metal complexes (10 μmol L^{-1}) in 0.1 mol L^{-1} phosphate buffer (pH 7.4) was irradiated with blue LED light (at 463 nm, 20 W) in the presence of APF (5 μmol

L^{-1}). To further validate this reaction, an additional control was prepared including 10 mmol L^{-1} D-mannitol as a hydroxyl radical scavenger. These data were similarly analyzed as earlier described for singlet oxygen.

Superoxide radical measurement. The capacity of the metal complexes, **MPD1** and **MPD2**, to generate superoxide anions was evaluated using the nitroblue tetrazolium (NBT) assay.[86] These experiments were carried out in phosphate buffer 0.1 mol L^{-1}, pH 7.4 at 25 °C. All electronic spectra were monitored for 70 minutes and recorded every 4 minutes, while these data were fit to a first-order kinetic equation. Superoxide production was monitored by changes in the absorbance at 590 nm,[61] which is an electronic band characteristic of formazan originating from the reaction of NBT with $O_2^{\bullet-}$. All measurements were set up using 100 μmol L^{-1} NBT and 10 to 60 μmol L^{-1} metal complexes with and without the biological reducing agent glutathione (1.5 mmol L^{-1}), which were also done in the dark or upon blue light irradiation. Controls were performed in the absence of the metal complexes or glutathione, and also with the addition of the enzyme superoxide dismutase (SOD, 4 U mL^{-1}), as well as in the presence and absence of light (blue).

Thermal and photochemical stability measurements

The stability of **MPD1** and **MPD2** at 25 μmol L^{-1} was investigated by monitoring this mixture in the dark. Electronic spectra of each sample were recorded in the UV-vis range in a 1 cm quartz cuvette containing 2 mL of solution. This monitoring was performed over a period of 2 hours (in acetonitrile, DMSO, 0.1 mol L^{-1} Tris-HCl buffer of pH 7.4 or methanol) and also over a period of 24 hours in 0.1 mol L^{-1} Tris-HCl buffer of pH 7.4. In addition, spectroscopic monitoring of the metal complexes was carried out upon irradiation with a blue LED (λ_{max} = 453 nm) in 0.1 mol L^{-1} Tris-HCl buffer of pH 7.4 for 2 hours.

Partition coefficients

This partition property was measured by following the well-established shake-flask method[103] in a non-miscible *n*-octanol/water mixture. The concentrations of the metal complexes (*ca.* 25 μmol L^{-1}, in 0.50% DMSO/water) were initially measured in water using a UV–Vis spectrophotometer and later mixed with an equal volume of *n*-octanol. This suspension was stirred for 24 hours in the dark at 25 °C, and then it was centrifuged for 5 minutes to achieve better phase separation. The aqueous layer was collected, and its electronic spectrum was obtained. A similar measurement was conducted for $\log D_{7.4}$, but with the aqueous solution being PBS buffer at pH 7.4. Then, the concentration of these metal complexes in water was calculated using standard curves (Abs *vs.* concentration), where the concentration in the *n*-octanol layer was calculated by the difference of the concentration found in the aqueous layer and expressed as $\log P$ and $\log D$ below.

$$P = \left(\frac{[\mathrm{Ru}]_{(\mathrm{octanol})}}{[\mathrm{Ru}]_{(\mathrm{Water})}}\right) \text{ and } D_{7.4} = \left(\frac{[\mathrm{Ru}]_{(\mathrm{octanol})}}{[\mathrm{Ru}]_{(\mathrm{PBS})}}\right)$$

where $[Ru]_{octanol}$ is the concentration of the ruthenium complex in *n*-octanol, and $[Ru]_{water}$ and $[Ru]_{octanol}$ are aqueous layers, after 24 h of shaking, as measured by UV–vis spectroscopy. These measurements were done at least twice.

Binding and photocleavage of DNA

DNA binding using electronic spectroscopy. All DNA binding measurements were performed with 10 μmol L^{-1} **MPD1** or **MPD2** in a conventional quartz cuvette containing 10 mmol L^{-1} Tris HCl buffer of pH 7.4. After each incremental addition of calf thymus DNA (10 μmol L^{-1} in base pairs), a 5-minute waiting time was implemented immediately before measurement by UV-Vis electron spectroscopy. The maximum volume of DNA solution added into the cuvette was carefully controlled to avoid significant dilution, which was always kept below 5% of the initial volume. A time course investigation was carried out previously showing that a much longer incubation time (2 to 3 h) did not show differences.

DNA binding using circular dichroism. To monitor the interaction of the metal compounds with calf or salmon DNA, circular dichroism (CD) spectroscopy was employed at 25 °C. These measurements were carried out in a solution of 10 mmol L^{-1} Tris HCl buffer of pH 7.4 in the presence of the compounds at increasing concentrations (5, 10, 20, 30 and 40 μmol L^{-1}) having a steady concentration of 100 μmol L^{-1} DNA. The spectra were recorded from 200 to 350 nm using a Jasco-815 instrument (Jasco) with a quartz cuvette of 1 cm path length. The data density was set to 1 nm, the scanning speed to 100 nm min^{-1}, and each measurement was the result of 5 accumulated spectra. This DNA–complex equilibrium was allowed to reach 60 min before starting the measurements.

DNA cleavage assay. This assay was carried out using plasmid pUC19 in 10 mmol L^{-1} Tris HCl buffer of pH 7.4, along with **MPD1** or **MPD2**, while $[Ru(bpy)_3]^{2+}$ was employed as a standard reagent. **MPD1** or **MPD2** was mixed with DNA at increasing concentrations (5, 10, 20, 30, 40 and 60 μmol L^{-1}), and incubated for 60 min at 25 °C, either in the dark or upon light irradiation (blue LED, $\lambda_{em\ max}$ = 463 nm, 1.7 W, Basetech Conrand) or redox stimulus (glutathione, 5 mmol L^{-1}). Then, all samples were applied in an agarose gel (0.8%), stained with Gel Red (1 μg m L^{-1} for 2 h), and the data were documented using a Gel Doc XR+ System (Bio-Rad), including a linear DNA ladder (1 kb, NEB) as one lane, and run in the TAE buffer, pH 8.0, by electrophoresis.

Size-exclusion assay. The size-exclusion assay was carried out by mixing 100 μmol L^{-1} salmon DNA with 200 μmol L^{-1} metal complexes in 10 mM Tris buffer, pH 7.4. Eluted samples consisting of excluded molecules were analyzed by UV-Vis electronic spectroscopy. Six samples were prepared containing (A) only the metal complex, (B) the metal complex with DNA (incubated for 1 h in the dark), (C) the metal complex with DNA (incubated for 4 h in the dark), (D) the metal complex with DNA (irradiated with blue light for 1 hour), (E) only DNA (incubated for 1 h), and (F) only DNA (incubated for 4 h). These samples were applied onto a Bio-Spin® P30 exclusion column (Bio-Rad) following the protocol described by the manufac-

turer. The Biospin P30 column (Bio-Rad) was previously prepared by performing the buffer exchange procedure and equilibrating the column with 10 mM Tris HCl buffer, pH 7.4, as described by the manufacturer. Then, 70 μL of each sample was applied onto the Biospin P30 column (Bio-Rad) and centrifuged at 1000*g* for 4 minutes. Excluded samples were collected in a microcentrifuge tube and electronic spectra were recorded after dilution to a final equal volume of 140 μL in Tris buffer.

Antibacterial measurements

Microorganisms and culture conditions. In this study, four bacterial strains were used: *Staphylococcus aureus* ATCC 25923 and ATCC 700698, *Staphylococcus epidermidis* ATCC 35984 and ATCC 12228, *Pseudomonas aeruginosa* ATCC 10145 and *Escherichia coli* ATCC 11303, all from the American Type Culture Collection (ATCC). All strains were inoculated in TSA plates and incubated for 24 h at 37 °C and then individual colonies were subcultured in 5 mL of MHB (Mueller-Hinton Broth) and incubated for 18–24 h at 37 °C. Briefly, the bacterial culture was adjusted to a final concentration of 10^6 colony-forming units (cfu) per mL.

Antibacterial assay. The bacterial susceptibility to ruthenium complexes was measured using minimal inhibitory concentration (MIC) and minimum bactericidal concentration (MBC) assays. MIC and MBC values were determined by the microdilution method using 96-well microtiter plates according to the Clinical and Laboratory Standards Institute. Bacterial suspensions previously adjusted to 10^6 cfu mL^{-1} were added into the 96-well plates and then **MPD1** and **MPD2** at concentrations ranging from 3.9 to 250.0 μg mL^{-1} diluted in MHB containing 2% DMSO were added to the wells. The plates were subjected to irradiation with a 96-array of blue LEDs for 1 h (8 mW cm^{-2}) or kept in the dark and then incubated at 37 °C for 24 h. After visualization of the plates, MIC values correspond to the compound concentration at which there is no visible growth. For MBC determination, 10 μL of aliquot from each well without visible growth was inoculated into TSA plates and incubated at 37 °C for 24 h. MBC was considered the lowest ruthenium complex concentration at which no colony growth was observed. The antimicrobial assays were performed in triplicate in three independent experiments.

Cytotoxicity measurements

Cell culture. The cells of the MDA-MB-231 (human triple-negative breast adenocarcinoma of mesenchymal phenotype, ATCC HTB-26), A549 (human lung alveolar epithelial basal cell adenocarcinoma, ATCC CCL-185) and MRC-5 (human non-tumorous lung, ATCC CCL-171) lines were cultured in Dulbecco's Modified Eagle's Medium (DMEM), supplemented with 10% fetal bovine serum (FBS). The A2780 cell line (human ovarian adenocarcinoma) was grown in RPMI 1640 medium (Roswell Park Memorial Institute), supplemented with 10% fetal bovine serum (FBS). The cell lines were kept in a humidified incubator under a CO_2 atmosphere (5%) at 37 °C.

Determination of cytotoxic activity. The cytotoxicity of the compounds was determined using the MTT (3-(4,5-dimethylthiazol-2-yl)-2,5-diphenyltetrazolium bromide) colorimetric method.[104] Initially, the cells were trypsinized to count and adjust the cell concentration, and then seeded in 96-well culture plates (1.5×10^4 per well, 150 μL) and subsequently incubated at 37 °C under 5% CO_2 for 24 h. After this period, the compounds were added at different concentrations (0.012 to 50 μmol L^{-1}), containing a final concentration of 0.5% DMSO, and the plates were kept in an incubator for a further 48 h and 72 h. After this period, 50 μL of MTT (1.0 mg mL^{-1} in PBS) was added to each well, which was then incubated in the incubator for a period of 3 h.

For the irradiation experiments, the 96-well plates were initially seeded and incubated for 24 h. The compounds were added and the plates were kept in the incubator for a further 24 h (37 °C and 5% CO_2). The culture medium was replaced with fresh medium without phenol red, and the plates were irradiated for 10 min and kept in the incubator for a further 24 h (λ_{irrad} = 460–465 nm, 18 mW cm^{-2}, 10.8 J cm^{-2}). After this period, 50 μL of MTT (1.0 mg mL^{-1} in PBS) was added to each well, and the plates were incubated for a period of 3 h. In both experiments, the formazan crystals formed were solubilized by adding 150 μL of DMSO, and the absorbance was recorded at 540 nm using a Synergy/H1-Biotek spectrophotometer/fluorimeter. The negative control cells were also cultivated with a medium containing 0.5% DMSO. The IC_{50} values were calculated using GraphPad Prism 8 software.

Author contributions

F. M. S. A.: conception of experiments, synthesis, chemical investigations and writing of the original draft; F. S. G. J.: investigation and theoretical calculations; G. F. S. O. and A. C. S. G.: investigation and biochemical measurements; A. L. A. and M. A. V.: investigation and analysis of antibacterial data; A. P. A.: X-ray data, analysis, and discussion; I. M. M. C.: analysis of data, writing and discussion; C. A. F. M.: MS data measurements and analysis; M. V. P. M. and A. A. B.: cytotoxicity data measurements and discussion; L. G. F. L.: conceptualization, supervision, funding acquisition, and writing; E. H. S. S.: conceptualization, data analysis, supervision, funding acquisition and writing.

Data availability

The data supporting this article have been included as part of the ESI.†

Conflicts of interest

There are no conflicts to declare.

Acknowledgements

The authors are thankful to CAPES (Finance code 001, PROEX 23038.000509/2020-82), CNPq (Universal 403838/2021-5; Universal 403447/2023-2; 441090/2023-0), FUNCAP (07/2021, PS1-0186-00087.01.00/21), Finep (CV. 01.22.0174.00), INCT tuberculose, a researcher grant to L. G. F. Lopes (CNPq # 302756/2022-1) and E. H. S. Sousa (CNPq #309010/2021-7). M. V. P.-M. thanks the São Paulo State Research Support Foundation (FAPESP, Process 2021/01787-0). We are also thankful to CENAPAD-UFC for allowing us to use the calculation facility for DFT and CENAUREM(UFC) for providing access to NMR equipment.

References

1 Word Heath Organization, *WHO Library Cataloguing-in-Publication Data Global Action Plan on Antimicrobial Resistance*, 2015.
2 M. Jampani and S. J. Chandy, *Health Sci. Rep.*, 2021, **4**, 1–3.
3 R. Nieuwlaat, L. Mbuagbaw, D. Mertz, L. L. Burrows, D. M. E. Bowdish, L. Moja, G. D. Wright and H. J. Schünemann, *Clin. Infect. Dis.*, 2021, **72**, 1657–1659.
4 G. P. Jorge, I. C. R. dos S. Goes and M. T. P. Gontijo, *Curr. Infect. Dis. Rep.*, 2022, **24**, 187.
5 J. O'Neill, *Tackling Drug-Resistant Infections Globally: Final Report and Recommendations. The Review on Antimicrobial Resistance*, 2016.
6 World Health Organization, *Interagency Coordination Group on Antimicrobial Resistance*, 2019, pp. 1-28.
7 I. D. Khan, K. S. Rajmohan, A. K. Jindal, R. M. Gupta, S. Khan, M. Shukla, S. Singh, Sh. Mustafa, A. Tejus and S. Narayanan, *Int. J. Med. Med. Res.*, 2017, **3**, 39–44.
8 C. Zampaloni, P. Mattei, K. Bleicher, L. Winther, C. Thäte, C. Bucher, J. M. Adam, A. Alanine, K. E. Amrein, V. Baidin, C. Bieniossek, C. Bissantz, F. Boess, C. Cantrill, T. Clairfeuille, F. Dey, P. Di Giorgio, P. du Castel, D. Dylus, P. Dzygiel, A. Felici, F. García-Alcalde, A. Haldimann, M. Leipner, S. Leyn, S. Louvel, P. Misson, A. Osterman, K. Pahil, S. Rigo, A. Schäublin, S. Scharf, P. Schmitz, T. Stoll, A. Trauner, S. Zoffmann, D. Kahne, J. A. T. Young, M. A. Lobritz and K. A. Bradley, *Nature*, 2024, **625**, 566–571.
9 K. S. Pahil, M. S. A. Gilman, V. Baidin, T. Clairfeuille, P. Mattei, C. Bieniossek, F. Dey, D. Muri, R. Baettig, M. Lobritz, K. Bradley, A. C. Kruse and D. Kahne, *Nature*, 2024, **625**, 572–577.
10 S. Chai, Y. Xie and L. Yang, *Curr. Opin. Solid State Mater. Sci.*, 2022, **26**, 1–12.
11 A. Frei, J. Zuegg, A. G. Elliott, M. Baker, S. Braese, C. Brown, F. Chen, C. G. Dowson, G. Dujardin, N. Jung, A. P. King, A. M. Mansour, M. Massi, J. Moat, H. A. Mohamed, A. K. Renfrew, P. J. Rutledge, P. J. Sadler, M. H. Todd, C. E. Willans, J. J. Wilson, M. A. Cooper and M. A. T. Blaskovich, *Chem. Sci.*, 2020, **11**, 2627–2639.
12 A. Frei, A. D. Verderosa, A. G. Elliott, J. Zuegg and M. A. T. Blaskovich, *Nat. Rev. Chem.*, 2023, **7**, 202–224.
13 W. W. Qin, Y. L. Li, Z. H. Zhu, H. L. Wang, L. Cheng and H. H. Zou, *Inorg. Chem.*, 2024, **63**, 16740–16749.
14 Z. H. Zhu, Y. Liu, C. Song, Y. Hu, G. Feng and B. Z. Tang, *ACS Nano*, 2022, **16**, 1346–1357.
15 Y. L. Li, J. F. Ai, Z. C. Chen, H. L. Wang, Z. H. Zhu, F. P. Liang and H. H. Zou, *ACS Mater. Lett.*, 2023, **5**, 1317–1331.
16 J. Wang, Y. Wang, D. Zhang, W. Ren and Z. Yang, *J. Colloid Interface Sci.*, 2022, **623**, 182–195.
17 X. Zhao, S. Wang, D. Shan, Y. Xu, L. Wu, H. Guo, G. Che, C. Liu and J. Du, *Chem. Eng. J.*, 2024, **495**, 1–14.
18 A. Lacueva-Aparicio, V. J. González, A. R. Remacha, D. Woods, E. Prado, I. Ochoa, S. Oliván and E. Vázquez, *Nanoscale Horiz.*, 2024, **9**, 990–1001.
19 B. M. Amos-Tautua, S. P. Songca and O. S. Oluwafemi, *Molecules*, 2019, **24**, 1–28.
20 N. Malatesti, I. Munitic and I. Jurak, *Biophys. Rev.*, 2017, **9**, 149–168.
21 R. R. Allison and K. Moghissi, *Photodiagn. Photodyn. Ther.*, 2013, **10**, 331–341.
22 A. Vaidya, Y. Sun, T. Ke, E. K. Jeong and Z. R. Lu, *Magn. Reson. Med.*, 2006, **56**, 761–767.
23 Z. Zhu, L. Wang, Y. Peng, X. Chu, L. Zhou, Y. Jin, H. Guo, Q. Gao, J. Yang, X. Wang, Z. Long, Y. Ge, S. Lu and B. Wang, *Adv. Funct. Mater.*, 2022, **32**, 2–18.
24 L. P. Rosa, F. C. da Silva, R. L. Vieira, B. R. Tanajura, A. G. da Silva Gusmão, J. M. de Oliveira, N. A. C. dos Santos and V. S. Bagnato, *Photodiagn. Photodyn. Ther.*, 2017, **19**, 235–238.
25 T. Maisch, R. M. Szeimies, G. Jori and C. Abels, *Photochem. Photobiol. Sci.*, 2004, **3**, 907–917.
26 S. P. Songca and Y. Adjei, *Int. J. Mol. Sci.*, 2022, **23**, 1–25.
27 X. Hu, Y. Y. Huang, Y. Wang, X. Wang and M. R. Hamblin, *Front. Microbiol.*, 2018, **9**, 1299.
28 F. Alves, E. T. P. Ayala and S. Pratavieira, *J. Photochem. Photobiol.*, 2021, **7**, 1–9.
29 Y. Liu, R. Qin, S. A. J. Zaat, E. Breukink and M. Heger, *J. Clin. Transl. Res.*, 2015, **1**, 140–167.
30 H. S. Kim and H. K. Seo, *Investig. Clin. Urol.*, 2021, **62**, 361–377.
31 S. Monro, K. L. Colón, H. Yin, J. Roque, P. Konda, S. Gujar, R. P. Thummel, L. Lilge, C. G. Cameron and S. A. McFarland, *Chem. Rev.*, 2019, **119**, 797–828.
32 T. Ezhilarasu, A. Sathiyaseelan, P. T. Kalaichelvan and S. Balasubramanian, *J. Mol. Struct.*, 2017, **1134**, 265–277.
33 A. A. Massoud, Y. M. Gohar, V. Langer, P. Lincoln, F. R. Svensson, J. Jänis, S. T. Gårdebjer, M. Haukka, F. Jonsson, E. Aneheim, P. Löwenhielm, M. A. M. Abu-Youssef and L. R. Öhrström, *New J. Chem.*, 2011, **35**, 640–648.
34 A. R. Biju, M. V. Rajasekharan, S. S. Bhat, A. A. Khan and A. S. Kumbhar, *Inorg. Chim. Acta*, 2014, **423**, 93–97.
35 J. Li, R. Liu, J. Jiang, X. Liang, L. Huang, G. Huang, H. Chen, L. Pan and Z. Ma, *Molecules*, 2019, **24**, 1–27.

36 Y. Wen, C. Ouyang, Q. Li, T. W. Rees, K. Qiu, L. Ji, H. Chao and H. Chao, *Dalton Trans.*, 2020, **49**, 7044–7052.
37 J. Li, R. Liu, J. Jiang, X. Liang, G. Huang, D. Yang, H. Chen, L. Pan and Z. Ma, *J. Inorg. Biochem.*, 2020, **210**, 1–13.
38 H. Huang, S. Banerjee, K. Qiu, P. Zhang, O. Blacque, T. Malcomson, M. J. Paterson, G. J. Clarkson, M. Staniforth, V. G. Stavros, G. Gasser, H. Chao and P. J. Sadler, *Nat. Chem.*, 2019, **11**, 1041–1048.
39 A. Jain, C. Slebodnick, B. S. J. Winkel and K. J. Brewer, *J. Inorg. Biochem.*, 2008, **102**, 1854–1861.
40 B. Z. Momeni and V. Noroozi, *Monatsh. Chem.*, 2017, **148**, 893–900.
41 R. N. Garner, C. G. Pierce, C. R. Reed and W. W. Brennessel, *Inorg. Chim. Acta*, 2017, **461**, 261–266.
42 J. N. Jaworski, C. V. Kozack, S. J. Tereniak, S. M. M. Knapp, C. R. Landis, J. T. Miller and S. S. Stahl, *J. Am. Chem. Soc.*, 2019, **141**, 10462–10474.
43 R. M. Silverstein, F. X. Webster and D. J. Kiemle, *Spectrometric Identification of Organic Compunds*, John Wiley e Sons, New York-USA, 7th edn, 2012.
44 D. L. Pavia, G. M. Lampman, G. S. Kriz and J. R. Vyvyan, *Introduction to Spectroscopy*, Cegangage Learning, Stanford, CT, USA, 5th edn, 2013.
45 S. Kelch and M. Rehahn, *Macromolecules*, 1999, **32**, 5818–5828.
46 J. M. Rao, M. C. Hughes and D. J. Macero, *Inorg. Chimica Acta*, 1976, **16**, 231–236.
47 N. Yoshikawa, T. Matsumura-Inoue, N. Kanehisa, Y. Kai, H. Takashima and K. Tsukahara, *Anal. Sci.*, 2004, **20**, 1639–1644.
48 P. Salvatore, A. Glargaard Hansen, K. Moth-Poulsen, T. Bjørnholm, R. John Nichols and J. Ulstrup, *Phys. Chem. Chem. Phys.*, 2011, **13**, 14394–14403.
49 D. E. Morris, K. W. Hanck and M. Keith Dearmond, *J. Electroanal. Chem. Interfacial Electrochem.*, 1983, **149**, 115.
50 P. Kulkarni, S. Padhye, E. Sinn, C. E. Anson and A. K. Powell, *Inorg. Chim. Acta*, 2002, **332**, 167–175.
51 Y. Wang, W. Perez, G. Y. Zheng and D. P. Rillema, *Inorg. Chem.*, 1998, **37**, 2051–2059.
52 P. Ford, D. F. P. Rudd, R. Gaunder and H. Taube, *J. Am. Chem. Soc.*, 1968, **90**, 1187–1194.
53 S. Estalayo-Adrián, S. Blasco, S. A. Bright, G. J. McManus, G. Orellana, D. C. Williams, J. M. Kelly and T. Gunnlaugsson, *ACS Appl. Bio Mater.*, 2021, **4**, 6664–6681.
54 D. L. Ma, T. Y. T. Shum, F. Zhang, C. M. Che and M. Yang, *Chem. Commun.*, 2005, 4675–4677.
55 X. Liu, B. Testa and A. Fahr, *Pharm. Res.*, 2011, **28**, 962–977.
56 M. M. Lerch, M. J. Hansen, G. M. van Dam, W. Szymanski and B. L. Feringa, *Angew. Chem.*, 2016, **128**, 11140–11163.
57 A. Juris, V. Balzani, F. Barigelletti, S. Campagna, P. Belser and A. Von Zelewsky, *Coord. Chem. Rev.*, 1988, **84**, 85–277.
58 S. Kim, M. Fujitsuka and T. Majima, *J. Phys. Chem. B*, 2013, **117**, 13985–13992.
59 F. Qu, R. W. Lamb, C. G. Cameron, S. Park, O. Oladipupo, J. L. Gray, Y. Xu, H. D. Cole, M. Bonizzoni, Y. Kim, S. A. McFarland, C. E. Webster and E. T. Papish, *Inorg. Chem.*, 2021, **60**, 2138–2148.
60 M. G. Espey, D. D. Thomas, K. M. Miranda and D. A. Wink, *Proc. Natl. Acad. Sci. U. S. A.*, 2002, **99**, 11127–11132.
61 H. Zhang, E. Agardh and C.-D. Agardh, *Graefe's Arch. Clin. Exp. Ophthalmol.*, 1993, **231**, 178–183.
62 W. M. T. Q. De Medeiros, M. J. C. De Medeiros, E. M. Carvalho, J. A. De Lima, V. S. Da Oliveira, A. C. F. B. De Pontes, F. O. N. Da Silva, J. A. Ellena, H. A. O. De Rocha, E. H. S. De Sousa and D. L. De Pontes, *RSC Adv.*, 2018, **8**, 16873–16886.
63 Z. Deng, P. Gao, L. Yu, B. Ma, Y. You, L. Chan, C. Mei and T. Chen, *Biomaterials*, 2017, **129**, 111–126.
64 S. V. Petersen and J. J. Enghild, *Biomed. Pharmacother.*, 2005, **59**, 175–182.
65 M. Deponte, *Biochim. Biophys. Acta, Gen. Subj.*, 2013, **1830**, 3217–3266.
66 B. Nordén, A. Rodger and T. Dafforn, *Linear dichroism and circular dichroism: a textbook on polarized-light spectroscopy*, Royal Society of Chemistry, Cambridge, UK, 1st edn, 2010.
67 A. K. Nayak, A. Mishra, B. S. Jena, B. K. Mishra and U. Subudhi, *Sci. Rep.*, 2016, **6**, 1–11.
68 K. Karidi, A. Garoufis, A. Tsipis, N. Hadjiliadis, H. Den Dulk and J. Reedijk, *Dalton Trans.*, 2005, 1176–1187.
69 J. Li, H. Yan, Z. Wang, R. Liu, B. Luo, D. Yang, H. Chen, L. Pan and Z. Ma, *Dalton Trans.*, 2021, **50**, 8243–8257.
70 D. D. Li, F. P. Huang, G. J. Chen, C. Y. Gao, J. L. Tian, W. Gu, X. Liu and S. P. Yan, *J. Inorg. Biochem.*, 2010, **104**, 431–441.
71 M. V. Palmeira-Mello, A. B. Caballero, A. Lopez-Espinar, G. P. Guedes, A. Caubet, A. M. T. de Souza, M. Lanznaster and P. Gamez, *J. Biol. Inorg. Chem.*, 2021, **26**, 727–740.
72 G. F. Brooks, K. C. Carroll, J. S. Butel, S. A. Morse and T. A. Mietzner, *Microbiologia Médica de Jawetz Melnick y Adelberg*, AMGH Editora, 26th edn, 2014.
73 H. P. Rang, M. M. Dale, J. M. Ritter, R. J. Flower and G. Henderson, *Rang & Dale's pharmacology*, Elsevier Health Sciences, 2011.
74 A. J. Vidyarthi, A. Das and R. Chaudhry, *Drug Discoveries Ther.*, 2021, **15**, 124–129.
75 Z. Deng, P. Gao, L. Yu, B. Ma, Y. You, L. Chan, C. Mei and T. Chen, *Biomaterials*, 2017, **129**, 111–126.
76 V. V. Pavlishchuk and A. W. Addison, *Inorg. Chim. Acta*, 2000, **298**, 97–102.
77 A. Sil, U. Ghosh, V. K. Mishra, S. Mishra and S. K. Patra, *Inorg. Chem.*, 2019, **58**, 1155–1166.
78 I. F. Eckhar and L. A. Summers, *J. Am. Chem. Soc.*, 1950, **26**, 2727–2735.
79 R. Ziessel, V. Grosshenny, M. Hissler and C. Stroh, *Inorg. Chem.*, 2004, **43**, 4262–4271.

80 Bruker AXS Inc, 2021, preprint.
81 L. Krause, R. Herbst-Irmer, G. M. Sheldrick and D. Stalke, *J. Appl. Crystallogr.*, 2015, **48**, 3–10.
82 L. Krause, R. Herbst-Irmer, G. M. Sheldrick and D. Stalke, *J. Appl. Crystallogr.*, 2015, **48**, 3–10.
83 O. v. Dolomanov, L. J. Bourhis, R. J. Gildea, J. A. K. Howard and H. Puschmann, *J. Appl. Crystallogr.*, 2009, **42**, 339–341.
84 G. M. Sheldrick, *Acta Crystallogr., Sect. A: Found. Adv.*, 2015, **71**, 3–8.
85 G. M. Sheldrick, *Acta Crystallogr., Sect. A: Found. Adv.*, 2015, **71**, 3–8.
86 A. L. Spek, *Acta Crystallogr., Sect. C: Struct. Chem.*, 2015, **71**, 9–18.
87 C. F. Macrae, I. Sovago, S. J. Cottrell, P. T. A. Galek, P. McCabe, E. Pidcock, M. Platings, G. P. Shields, J. S. Stevens, M. Towler and P. A. Wood, *J. Appl. Crystallogr.*, 2020, **53**, 1–10.
88 A. L. Spek, *J. Appl. Crystallogr.*, 2003, **36**, 7–13.
89 R. A. Gaussian, M. Frisch, G. Trucks, H. Schlegel, G. Scuseria, M. Robb, J. Cheeseman, G. Scalmani, V. Barone, B. Mennucci and G. Petersson, Inc., Wallingford CT, 2009.
90 A. D. Becke, *J. Chem. Phys.*, 1993, **98**, 5648–5652.
91 P. J. Stephens, F. J. Devlin, C. F. Chabalowski and M. J. Frisch, *J. Phys. Chem.*, 1994, **98**, 1–5.
92 C. Lee, W. Yang and R. G. Parr, *Phys. Rev. B: Condens. Matter Mater. Phys.*, 1988, **37**, 785–789.
93 P. J. Hay and W. R. Wadt, *J. Chem. Phys.*, 1985, **82**, 299–310.
94 W. R. Wadt and P. J. Hay, *J. Chem. Phys.*, 1985, **82**, 284–298.
95 G. Frenking and W. Koch, *J. Chem. Phys.*, 1986, **84**, 3224–3229.
96 B. Mennucci, E. Cancè and J. Tomasi, *J. Phys. Chem. B*, 1997, **101**, 10506–10517.
97 T. Lu and F. Chen, *J. Comput. Chem.*, 2012, **33**, 580–592.
98 N. M. O'Boyle, A. L. Tenderholt and K. M. Langner, *J. Comput. Chem.*, 2008, **29**, 839–845.
99 H. Y. Ding, X. S. Wang, L. Q. Song, J. R. Chen, J. H. Yu, C. Li and B. W. Zhang, *J. Photochem. Photobiol., A*, 2006, **177**, 286–294.
100 H. Y. Ding, X. S. Wang, L. Q. Song, J. R. Chen, J. H. Yu, C. Li and B. W. Zhang, *J. Photochem. Photobiol., A*, 2006, **177**, 286–294.
101 X. F. Zhang and X. Li, *J. Lumin.*, 2011, **131**, 2263–2266.
102 C. Tanielian, C. Wolff and M. Esch, *J. Phys. Chem.*, 1996, **100**, 6555–6560.
103 S. Roy, E. Colombo, R. Vinck, C. Mari, R. Rubbiani, M. Patra and G. Gasser, *ChemBioChem*, 2020, **21**, 2966–2973.
104 T. Mosmann, *J. Immunol. Methods*, 1983, **65**, 55–63.